Title
ATOMIC MECHANISMS OF PRECIPITATE PLATE GROWTH

Authors
Howe, J.M.
Dahmen, U.
Gronsky, R.

Publication Date
1986-06-01

Lawrence Berkeley Laboratory
UNIVERSITY OF CALIFORNIA

Materials & Molecular Research Division

Submitted to Philosophical Magazine, A

ATOMIC MECHANISMS OF PRECIPITATE PLATE GROWTH

J.M. Howe, U. Dahmen, and R. Gronsky

June 1986

Prepared for the U.S. Department of Energy under Contract DE-AC03-76SF00098

DISCLAIMER

ATOMIC MECHANISMS OF PRECIPITATE PLATE GROWTH

J.M. Howe

Department of Metallurgical Engineering and Materials Science,
Carnegie-Mellon University,
Pittsburgh, PA 15213

U. Dahmen and R. Gronsky

National Center for Electron Microscopy,
Materials and Molecular Research Division,
Lawrence Berkeley Laboratory,
University of California,
Berkeley, CA 94720

TABLE OF CONTENTS

ABSTRACT

In this investigation, the techniques of high-resolution transmission electron microscopy, image simulations, energy-dispersive x-ray spectroscopy and convergent-beam electron diffraction are used to characterize the atomic structure, chemistry and growth mechanisms of γ' plate-shaped precipitates in an Al-4.2 at.% Ag alloy aged for 30 min. at 350°C. The results of these studies show that γ' precipitates have the composition Ag_2Al and are ordered during the early stages of growth, where the A-planes in the h.c.p. precipitates contain nearly pure Ag and the B-planes have the composition Al_2Ag. In addition, the precipitate/matrix interphase boundary is largely coherent and faceted along low-energy precipitate/matrix directions and both the lengthening and thickening of γ' plates occur by a terrace-ledge-kink mechanism, where the limiting step in the growth process appears to be the substitutional diffusion of Ag atoms across kinks in the Shockley partial dislocation ledges which terminate in the Ag-rich, A-planes. The complementary information obtained from each of these techniques allows the mechanisms of precipitate plate growth to be understood at the atomic level.

1. INTRODUCTION

The interfacial structures and growth kinetics of metastable γ' and equilibrium γ (Ag_2Al) precipitate plates in Al-Ag alloys have been extensively studied by conventional and *in-situ* transmission electron microscopy (TEM) techniques, because the α(f.c.c.) $\rightarrow$ γ(h.c.p.) transformation is one of the simpler diffusional transformations involving a distinct change in crystal structure (Hren and Thomas 1963, Nicholson and Nutting 1961, Laird and Aaronson 1967, Laird and Aaronson 1969). This system also serves as an ideal model with which to test a theory of precipitate morphology (Aaronson 1962) for growth of (semi)coherent precipitates by a ledge mechanism, as explored in many previous publications (Laird and Aaronson 1969, Ferrante and Doherty 1976, Aaronson, Laird and Kinsman 1970). Although these studies have provided considerable insight into the morphological development and growth kinetics of plate-shaped precipitates, there is still considerable controversy regarding the structures and migration processes of the various precipitate interfaces (Chen and Doherty 1977, Aaronson 1977, Rajab and Doherty 1982, Sagoe-Crentsil and Brown 1984, Aaronson 1979, Reynolds, Enomoto and Aaronson 1984).

Improvements in the high-resolution and probe-forming capabilities of TEM now provide the opportunity to study precipitation processes in metals at much higher resolution than was previously possible. For example, recent high-resolution TEM analyses of γ' precipitates in the Al-Ag system allowed Howe, Aaronson and Gronsky (1985a,b) to determine that growth of both the faces and edges of these plates occurs by similar ledge mechanisms, where the ledges are multiples of two Shockley partial dislocations in height. In addition, the terraces between the ledges are atomically flat and uniformly stepped-down from the centers to the edges of precipitates as predicted by theory. Although these authors further proposed that both the edges of γ' precipitates and ledges on the faces may grow by similar kink mechanisms, they were not able to determine the atomic-level processes involved in the transformation. The purpose of the present research is to perform highly detailed analyses of both the structural and chemical components required for growth of γ' plate-shaped precipitates in an Al-Ag alloy, using high-resolution TEM, image simulations, energy-dispersive x-ray spectroscopy (EDS) and convergent-beam electron diffraction (CBED). Each provides different structural and chemical information, and this combination of techniques was chosen in order to understand the mechanisms of precipitate growth at the atomic level.

2. EXPERIMENTAL PROCEDURES

2.1 Material and Heat Treatment

An Al-4.2 at.% Ag alloy was vacuum melted and cast, using Al and Ag of 99.99% purity. The ingot was homogenized at 535°C for about 40 hrs. to reduce segregation, and hot and cold rolled to 180 μm final thickness. Discs of 2.3 mm diameter were punched from the sheets, solution annealed for 30 min. at 550°C, quenched in cold water, aged for 30 min. at 350°C and again quenched in cold water.

2.2 Electropolishing and Ion-Beam Milling

The aged specimens were polished in a twin-jet Fischione apparatus using a 25% nitric - 75% methanol electrolyte at around -30 to -40°C. The voltage and current were about 14-20 V and 15-35 mA, respectively. After perforation, the thin foils were rinsed in three methanol baths, dried and stored under vacuum. Ion-beam milling of thin foils was found to facilitate high-resolution imaging by removing a thin oxide which inevitably formed on the surfaces of the foils during polishing. In order to avoid heating during milling, thin foils were either milled at liquid-nitrogen temperature, or alternately milled and cooled in 30 sec. intervals using a 4 keV accelerating voltage, a 0.3 mA gun current and a 12° tilt.

2.3 High-Resolution Transmission Electron Microscopy

High-resolution TEM images were taken on a JEOL 200CX microscope, equipped with a LaB_6 filament and operating at 200 keV. Specimens were tilted into exact $\langle 110\rangle//\langle 11\bar{2}0\rangle$ or $\langle 111\rangle//\langle 0001\rangle$ orientations using the top-entry, high-resolution goniometer. Objective apertures with radii of either 0.64 or 0.74 $\mathring{A}^{-1}$ were used to filter out high-order spatial frequencies and improve image contrast. Through-focus series of images were taken in 120 $\mathring{A}$ increments, starting at the minimum contrast condition and continuing to the third pass band. Amorphous edges were included in the images for optical diffraction analyses. For the JEOL 200CX at 200 keV, C_s = 1.2 mm, C_c = 1.4 mm and therefore, Δz_{mc} = -240 $\mathring{A}$, Δz_{Sch} = -660 $\mathring{A}$, $\Delta z_{2nd\ pb}$ = -1290 $\mathring{A}$ and $\Delta z_{3rd\ pb}$ = -1690 $\mathring{A}$.

2.4 Image Simulations

Simulated high-resolution TEM images were calculated using the A.S.U. Multislice Programs described by O'Keefe and Buseck (1979) and modified into the ZOLZPROG series of programs by Spence (1980). The ZOLZPROG consists of three programs, FCO128, DEF128 and IM128, which are run in succession and use a 128 X 128 array to compute a simulated electron image. Images of γ' precipitates, the precipitate/matrix interface and Shockley partial dislocation ledges at the precipitate/matrix interface were calculated in a $\langle 110\rangle//\langle 11\bar{2}0\rangle$ orientation, using the lattice parameters for the precipitate and matrix given by Mondolfo (1979). The number of atoms per unit cell and values of DSMAX (the maximum value in reciprocal space of reflections included in the calculation) in the calculations varied from 2 and 4.0 for a simple h.c.p. unit cell, to 162 and 2.2 for the dislocation ledge, where the unit-cell dimensions in the projection plane were about 26 and 30 Å. The unit-cell dimension along the electron-beam direction was 2.864 Å, which was the value used for the phase-grating slice thickness. The number of beams used in the multislice calculations was equal to DSMAX/2, and the 0001 h.c.p. reflections were included in all of the calculations. The microscope parameters used in both the image calculations and contrast transfer function (CTF) program (Kilaas 1984) were C_s = 1.2 mm, a_i = 1.0 mrad, Δ = 50 Å, and $r_{obj\ ap}$ = 0.64 $Å^{-1}$.

2.5 Energy-Dispersive X-Ray Spectroscopy and Convergent-Beam Electron Diffraction

The γ' precipitates were extracted from the Al matrix and their composition was analyzed on a Philips EM400 equipped with a Kevex System 7000 analytical spectrometer, using the ratio method (Cliff and Lorimer 1975, Goldstein 1979) and an Ag_2Al standard. The CBED analyses were performed on the same Philips EM400, which also had a "free lens" control (Sarikaya and Thomas 1984) so that optimum convergence angles and probe diameters could be obtained on the samples. Detailed explanations of these procedures are presented by Howe and Gronsky (1985, 1986a) and Howe, Sarikaya and Gronsky (1986).

3. EXPERIMENTAL RESULTS AND DISCUSSION

3.1 High-Resolution Transmission Electron Microscopy

3.1.1 Atomic Models of Shockley Partial Dislocation Ledges in a <110>//<11$\bar{2}$0> Orientation

Figures 1(a) and (b) show the projected potentials for two different types of Shockley partial dislocation ledges which are likely to be found on the face of a γ' precipitate when it is viewed edge-on. The γ' precipitate plates thicken by the movement of these dislocation ledges along their faces on alternate {111} matrix planes, which accomplishes the f.c.c. → h.c.p. structural transformation necessary for growth (Howe et al. 1985b, Hren and Thomas 1963). The stacking sequences indicated in the precipitate and matrix on either side of the ledges in Figs. 1(a) and (b) illustrate this structural transformation. The dislocation ledge in Fig. 1(a) is commonly called a 90° Shockley partial dislocation, because its Burgers vector lies perpendicular to the electron beam. This type of dislocation can be pictured from a Thompson tetrahedron (Thompson 1953), if the electron beam is chosen to lie along the $[1\bar{1}0]$ direction and the Shockley partial dislocation has an $a/6[\bar{1}\bar{1}2]$ Burgers vector. The ledge in Fig. 1(b) is called a 30° Shockley partial dislocation ledge because its Burgers vector lies at an angle of 30° to the electron beam, i.e. either an $a/6[2\bar{1}\bar{1}]$ or $a/6[\bar{1}2\bar{1}]$ dislocation on the same reference tetrahedron. The atomic positions around the dislocation ledges in Figs. 1(a) and (b) were calculated using isotropic elastic theory as given by Hirth and Lothe (1960), and a computer program that was developed to calculate and output the atomic positions in proper format for the image simulations is given by Howe (1985).

Several simulated high-resolution TEM images of these ledges are shown in Figs. 1(c) through (f). In Figs. 1(c) and (d), the atomic positions of the precipitate, matrix and dislocation ledge are all visible as bright atomic columns on a dark background, allowing the atomic structure of the ledge to be determined. However, in Figs. 1(e) and (f), it is difficult to resolve the atomic positions at the edges of the ledges because alternate basal planes in the precipitate appear dark at this particular thickness and objective lens defocus. The reason that alternate basal planes in the precipitate appear dark is because the A-planes contain nearly pure Ag while the B-planes have only 33 at.% Ag with a balance of Al. While the origin of such ordering of Ag on alternate basal planes will be discussed in detail in a subsequent section, it should be noted here that this ordering can cause alternate basal planes in the precipitate to be indistinguishable above a dark background for certain values of specimen thickness and objective lens defocus.

Figure 2 illustrates two different types of Burgers circuits that can be used to distinguish between 90° and 30° Shockley partial dislocation ledges. One type of circuit is constructed in Figs. 2(a) and (b) and the second type of circuit is constructed in Figs. 2(c) and (d). Comparison between these two types of circuits shows that they differ only by the projected atom positions that are followed in the h.c.p. precipitate, behind the dislocation ledge. Also note that not all of the projected atom positions in these $\langle 110\rangle//\langle 11\bar{2}0\rangle$ models are coplanar, that is, every-other atom actually lies in a plane which is slightly above or below the plane of the figure. This allows the screw component of the 30° dislocation out of the plane of the figure to be identified. For example, the Burgers circuit in Fig. 2(d) translates out of the plane of the diagram as it traverses across every-other basal plane. Thus, it does not reveal the presence of the 30° Shockley partial dislocation ledge, which also lies out of the figure plane. However, if the circuit is constructed such that it remains coplanar, as in Fig. 2(b), the presence of the 30° dislocation is indicated by a closure failure. The opposite situation occurs for the 90° dislocation ledge in Figs. 2(a) and (c). In this case, the Burgers circuit which translates out of the plane of the diagram leads to a closure failure, since the Burgers vector lies in the plane of the figure.

Note that the closure failures in Figs. 2(b) and (c) are both $a/4\langle 112\rangle$ and therefore, do not represent the actual $a/6\langle 112\rangle$ and $a/12\langle 112\rangle$ closure failures associated with edge components of the 90° and 30° dislocation ledges, respectively. The reason that these circuits do not give the actual Burgers vectors of the dislocations is because the circuits do not start and finish in the plane of the dislocation on the h.c.p. side, as specified by Frank (1951). However, these types of Burgers circuits are useful for distinguishing between 90° and 30° dislocations at complicated precipitate interfaces.

3.1.2 Atomic Structure of Precipitate Faces in a $\langle 110\rangle//\langle 11\bar{2}0\rangle$ Orientation

As shown in Fig. 3, the 30 min. aging treatment at 350°C produced a relatively dense dispersion of well-developed γ' precipitates without the influence of a prior G.P. zone structure. Since the γ' plates precipitate on the four {111} matrix planes with the orientation relationship $\{111\}_{\alpha}//\{0001\}_{\gamma'}$ and $\langle 110\rangle_{\alpha}//\langle 11\bar{2}0\rangle_{\gamma'}$, two variants of the precipitates are edge-on in the $\langle 110\rangle//\langle 11\bar{2}0\rangle$ orientation shown in Fig. 3, while the other two variants are inclined with respect to the electron beam. Strain contrast from dislocation ledges on the faces of several inclined precipitates is visible in the upper-right corner of Fig. 3 (arrows). As indicated by the micron marker in this figure, the γ' pecipitates are on the order of one to several μm in diameter and about 100 to 300 Å thick.

Figure 4 shows an experimental high-resolution TEM image of a multiple-unit ledge on the face of a γ' precipitate plate. Previous studies (Howe et al. 1985a,b, Jones and Trivedi 1975, Atkinson 1982) have shown that elastic and diffusional interactions often cause single Shockley partial dislocation ledges on the precipitate faces to merge and form such multiple-unit ledges. Although it is difficult to distinguish the atomic positions at the ledge due to the particular thickness and defocus conditions in this image (compare with Figs. 1(e) and (f)), construction of the Burgers circuit in Fig. 2(b) indicates that four 30° Shockley partial dislocations are associated with this approximately ten-plane ledge. In addition, examination of the {111} matrix planes parallel to the precipitate face shows that they are continuous as they cross the multiple-unit ledge to become the {0001} precipitate planes and therefore, that the ledges are largely coherent in this orientation, as depicted in the models in Figs. 1(a) and (b). Slight displacement of these planes normal to the Burgers vectors of the ledge dislocations (perpendicular to the precipitate face) is also evident, as in the atomic models in Figs. 1(a) and (b). This type of displacement leads to the $\mathbf{g} \cdot \mathbf{b} \times \mathbf{u}$ contrast which is typically seen in strain contrast images of such dislocations (Hirsch, Howie, Nicholson, Pashley and Whelan 1977). Thus, from the matching between the calculated and experimental images of Shockley partial dislocation ledges in Figs. 1 and 4, it is possible to conclude that the structural transformation needed for growth of the γ' precipitates is accomplished by the passage of Shockley partial dislocations along alternate {111} matrix planes parallel to the faces, and that the growth interface (the ledges) is essentially coherent in this orientation.

3.1.3 Atomic Structure of Precipitate Edges in a <110>//<11$\bar{2}$0> Orientation

Figure 5 shows a high-resolution TEM image of a precipitate edge in a <110>//<11$\bar{2}$0> orientation. The jagged shape of the edge indicates that it is also composed of Shockley partial dislocations that have migrated across the precipitate faces and assumed a staggered configuration at the edge. Again, sighting along the {111} planes parallel to the faces shows that the edge is largely coherent, just as for the ledges on the faces described above, although there also appears to be evidence of one terminating fringe near the lower face of the precipitate, indicated by a ⊢ in Fig. 5. The {111}//{0001} planes also bend substantially in this area, indicating that there is greater strain along the precipitate edge than along the precipitate faces, which always appear to be perfectly coherent between the Shockley partial dislocation ledges. These structural observations agree with the lattice parameter changes for formation of γ' precipitates given by Mondolfo (1979), which suggest a negligible ($\sim$ 0.5%) expansion along the a-axis in the plane of the

precipitates and a 2.5% contraction along the c-axis, perpendicular to the faces. These image characteristics also agree with a precipitate edge that is modelled as being composed of Shockley partial dislocations which are stacked vertically, although it is difficult to distinguish the positions of the individual partial dislocations at the edge due to the complex nature of the interface. Also note that the precipitate edge in Fig. 5 is nearly flat, rather than having a semicircular or parabolic-cylinder shape, as is often assumed in kinetic analyses of precipitate lengthening (Trivedi 1982, Christian 1965, Aaronson, Lee and Russell 1977). This flat edge roughly parallels a {112} plane in the matrix.

Both types of Burgers circuits discussed in Fig. 2 were constructed around the precipitate edge in Fig. 5, in order to identify the types of dislocations present at the edge. The precipitate is forty-six {111} matrix planes thick (~ 106 Å), as indicated in the figure. When the Burgers circuit in Fig. 2(b) is constructed around the edge, a closure failure of fifteen lattice planes occurs, indicating the presence of fifteen 30° Shockley partial dislocations at the edge. Similarly, when the Burgers circuit in Fig. 2(c) is constructed around the edge, eight additional closure failures occur, indicating the presence of eight 90° Shockley partial dislocation ledges at the edge. Thus, a total of twenty-three partial dislocations are associated with the forty-six plane precipitate, giving excellent experimental evidence that growth is occurring by the passage of Shockley partial dislocations across alternate {111} matrix planes (Hren and Thomas 1963, Laird and Aaronson 1967, Howe et al. 1985a,b). Furthermore, the ratio of two 30° Shockley partials to every 90° partial dislocation supports the suggestion (Howe et al. 1985a,b) that equal numbers of all three types of Shockley partial dislocations are nucleated on alternate {111} planes during growth, in order to minimize the elastic strain energy at the precipitate edges. This is similar to the growth of θ' plates on {001} planes in Al-Cu alloys, where the partial dislocations that constitute ledges are of the type a/2<100>, and ledges are found to nucleate in pairs with equal and opposite Burgers vectors (Dahmen and Westmacott 1983a,b).

As illustrated in Fig. 6, a h.c.p. precipitate could thicken either by the nucleation and propagation of the same Shockley partial dislocations on alternate {111} planes, or by the incorporation of equal numbers of all three types of Shockley partial dislocations on alternate {111} matrix planes. If the f.c.c. → h.c.p. transformation is accomplished by the passage of identically oriented Shockley partial dislocations of the same type on every other (111) plane, then an overall shape change occurs, as shown in Fig. 6(a). This distortion must be accommodated within the matrix, resulting in a high strain energy at the precipitate edges. However, if the same transformation is accomplished by using equal numbers of all three

Shockley partials on (111), as illustrated in Fig. 6(b), then no shape change occurs. Such an arrangement is highly favored from a strain-energy viewpoint and consequently, the Shockley partial dislocations would be stacked vertically at the precipitate edges. The 2:1 ratio of 30° to 90° Shockley partial dislocations and the jagged shape of the precipitate edge in Fig. 5 indicate that the latter situation occurs.

3.1.4 Atomic Structure of Precipitate Edges in a <111>//<0001> Orientation

The structure of the precipitate edges was also examined in a <111>//<0001> orientation to search for important structural characteristics along the third dimension of the γ' precipitates. In order to obtain high-resolution images of the matrix in this orientation, it was necessary to employ the following tilted-illumination conditions. Figure 7(a) shows a $[111]_{\alpha}//[0001]_{\gamma'}$ diffraction pattern taken from the precipitate and surrounding matrix shown in Fig. 9. In this orientation, the six high-intensity spots surrounding the forward-scattered beam are the first-order $01\bar{1}0$ precipitate reflections, representing a lattice spacing of about 2.5 Å. An axial high-resoluton image of the precipitate can be obtained by centering a 0.64 $Å^{-1}$ objective aperture around these spots as shown in Fig. 7(b). However, the first-order matrix reflections in this orientation are the 220 spots, which coincide with the $11\bar{2}0$ precipitate reflections, as indicated in Fig. 7(a). These spots correspond to a 1.4 Å lattice spacing, and the corresponding planes can only be imaged by tilting the incident electron beam so that the 220 reflections are symmetrically positioned inside the objective aperture, as shown in Fig. 7(c). With this tilted-illumination condition, both the $\{01\bar{1}0\}$ and $\{11\bar{2}0\}$ planes are imaged in the precipitate, and the {220} planes are imaged in the matrix. Thus, a through-focus series of axial images was first taken to determine the atomic structure of the precipitate edges, and a second through-focus series of tilted-illumination images was then taken to examine the coherency of the $\{220\}//\{11\bar{2}0\}$ planes across the edges.

Figure 8 shows a bright-field TEM image of a γ' precipitate lying perpendicular to the electron beam in a <111>//<0001> orientation. Several crystallographic directions in the matrix are superimposed on the precipitate and six of its edges are numbered. These numbered edges are all parallel to <110> directions within the (111) matrix plane. In between the numbered edges, the precipitate edges parallel <112> directions, although facets are visible on all these segments (arrows). Laird and Aaronson (1969) have shown by *in-situ* TEM studies that similar γ plates lengthen by the movement of these facets parallel to the <110> edges rather than by the overall movement of the linear <110> edges. Thus, the structure of such facets is an important factor in determining the atomistics of the growth process.

A low-magnification axial image of several 150 Å facets along the edge of a similar γ' precipitate plate is shown in Fig. 9(a). Comparison with the crystallographic directions of the matrix superimposed on the figure shows that this precipitate edge also parallels a <112> direction overall, in this particular case $[\bar{1}\bar{1}2]$. In addition, this figure shows that the edges of the facets along the edge further parallel <110> directions in the matrix on a nearly atomic level. The corner in region A, between two facets in Fig. 9(a), is enlarged in Fig. 9(b). Note that this corner is not sharp but rounded, and that the rounded edge is actually faceted along <110> directions down to the single-atom level, as indicated by the small black dots in this figure. Such faceting at the atomic level demonstrates that the precipitates are highly crystallographic on both macroscopic and microscopic levels and therefore, that interfacial energy effects strongly influence the overall precipitate shape. That is, there is an extreme tendency for all interfaces of the precipitate to lie along low-energy $\langle 110\rangle // \langle 11\bar{2}0\rangle$ close-packed directions, presumably because this minimizes both the chemical and structural contributions to the interfacial energy (Alexander, LeGoues, Laughlin and Aaronson 1985).

Figure 10 shows an enlargement from a tilted-illumination image at the corner of a nearly hexagonal γ' precipitate. Sighting along the 1.4 Å {220} matrix planes reveals that they are continuous as they cross the precipitate/matrix interface to become the $\{11\bar{2}0\}$ pecipitate planes, thus demonstrating that the precipitate edges are also coherent with the matrix in the habit plane. Since ledges have often been observed to nucleate from the corners of pecipitate plates in *in-situ* TEM studies of γ plates, as well as in other alloy systems (Aaronson 1974), these corners have been proposed to act as large stress concentrators, which aid in the nucleation of new dislocations for growth. However, the high-resolution image in Fig. 10 indicates that the corners of γ' precipitates are entirely coherent, and that there is no obvious increase in the strain of the lattice planes at the corner.

That growth of precipitate edges occurs by the lateral migration of kinks in ledges parallel to <110> matrix directions rather than by the overall movement of a $\langle 110\rangle // \langle 11\bar{2}0\rangle$ interface normal to itself, is illustrated by the tilted-illumination, high-resolution image in Fig. 11(a). In this image, several single-atom ledges are spaced about 35 Å apart along along a precipitate edge, which parallels a <110> matrix direction on an atomic level. Note that the terraces between each of the ledges in Fig. 11(a) are atomically flat while the ledges (arrows) are indistinct, indicating that atomic attachment is occurring at the ledges. However, because each of these ledges actually represents a kink in a Shockley partial dislocation when all three dimensions of the precipitate are

considered, this image further suggests that growth of γ' precipitates occurs by the attachment of atoms to kinks in Shockley partial dislocations, which constitute the ledges on both the faces and edges of these precipitate plates. Thus, the standard terrace-ledge-kink mechanism of atomic attachment, which was originally proposed for the growth of close-packed interfaces of a solid into a liquid or vapor (Burton, Cabrera and Frank 1950, Rosenberg and Tiller 1957), appears to be equally valid for describing the growth of a close-packed solid of one crystal structure into another (Aaronson 1962), as illustrated in Fig. 11(b).

3.2 Quantitative Energy-Dispersive X-ray Analysis of Extracted Precipitates

Figure 12(a) shows a bright-field TEM image of two γ' precipitates lying face-down on a carbon film, typical of the extracted precipitates chosen for EDS analysis in this study. Figure 12(b) shows the x-ray spectrum obtained from the larger precipitate, and enlargements of the Al Kα and Ag Kα peaks which were used for quantification are shown in Figs. 12(c) and (d). The large Cu peak in Fig. 12(b) is due to fluorescence from the Cu grid supporting the carbon film. Analysis of ten precipitate spectra using the ratio method (Cliff and Lorimer 1975) and a value for $k_{\alpha AgAl}$ determined from an Ag_2Al standard yielded an average precipitate composition of 66.8 ± 3.8 at.% Ag (Howe and Gronsky 1986a). Thus, the composition of these metastable γ' precipitates is similar to the congruently-melting compound Ag_2Al present in the Al-Ag equilibrium phase diagram (Mondolfo 1979). This composition lies near the left side of the equilibrium γ phase field at 350°C, and is the composition usually assigned to equilibrium γ precipitates which form in Al-Ag alloys after extended high-temperature aging treatments.

3.3 Convergent-Beam Electron Diffraction of Precipitates in a <110>//<11$\bar{2}$0> Orientation

Evidence has appeared in several of the previous <110>//<11$\bar{2}$0> images which suggests that the γ' precipitates possess long-range order among alternate basal planes. For example, the matching between the calculated and experimental high-resolution TEM images in Figs. 1 and 4 was obtained by ordering of Ag atoms on alternate basal planes, a point which was only briefly mentioned when these figures were presented. Such order should lead to the appearance of kinematically forbidden 0001, l=odd precipitate reflections in diffraction patterns from precipitates, and these reflections were often found in the <110>//<11$\bar{2}$0> selected-area diffraction patterns recorded with the high-resolution images. However, the 0001, l=odd reflections can also appear due to double diffraction in the precipitate and therefore, caution must be exercised when deciding on the origin of these reflections (Smith, Bursill and Wood 1985, Howe and Gronsky 1986b). In

this study, CBED was used to determine whether the 0001, l=odd reflections are due to ordering or double diffraction.

Figure 13 shows two <110>//<11$\bar{2}$0> CBED patterns taken from different γ' precipitates located a short distance from one another in a thin foil. In Fig. 13(a), the 0001, l=odd reflections are strong and there is no evidence of Gjonnes-Moodie (G-M) lines (Gjonnes and Moodie 1965), indicating that the reflections are not kinematically or dynamically forbidden and therefore, that they are due to long-range order on alternate basal planes in the precipitate. However, the same 0001, l=odd reflections in Fig. 13(b) display clear G-M lines through their centers due to the presence of a c-glide plane, indicating that these reflections are kinematically forbidden and therefore, that this precipitate does not possess long-range order among alternate basal planes. These somewhat contradictory results can be explained if it is assumed that individual γ' precipitates possess various degrees of order, ranging from a highly-ordered arrangement of Ag and Al atoms on alternate basal planes to a disordered arrangement. This behavior is also consistent with the observation that γ' precipitates undergo an order/disorder transformation after prolonged aging at 350°C, as described by Hren and Thomas (1963). However, the majority of γ' precipitates in this study displayed a high degree of long-range order among alternate basal planes, as evidenced by the strong intensities of the 0001, l=odd reflections in most selected-area diffraction patterns.

In addition to the long-range order just described, some of the γ' precipitates displayed evidence of further order within the basal planes. For example, note the relatively weak reflections, which lie at one-third and two-thirds of the distance from the forward-scattered beam to the 11$\bar{2}$0 precipitate reflection, indicated by arrows in Fig. 7(a). These spots are symmetrically positioned throughout the diffraction pattern, and their diffuse character indicates that they may be due to short-range ordering within the basal planes. Neumann (1966) observed similar diffuse spots at the 1/3<11$\bar{2}$0> and 2/3<11$\bar{2}$0> positions in <0001> x-ray diffraction patterns from Ag_2Al single crystals which were aged for 10 days at 180°C. Based upon this data, Neumann (1966) constructed a model for short-range order within the basal planes, where each Al atom is surrounded by six Ag atoms, giving an overall composition of 66 at.% Ag. A similar arrangement of atoms will be used for constructing an atomic model for the γ' precipitates in this study, except that the ordered basal planes in these precipitates contain only aout 33 at.% Ag and therefore, each Ag atom is surrounded by six Al atoms.

3.4 Atomic Model for Precipitates

A possible atomic model for the γ' precipitate structure was constructed from the previous information about the composition and ordering within the γ' precipitates, and is shown in Fig. 14. In this model, the A-planes are composed of pure Ag while the B-planes have the composition Al_2Ag, in order to account for the 0001, l=odd long-range order reflections in the <110>//<11$\bar{2}$0> diffraction patterns. In addition, each Ag atom is surrounded by six Al atoms within the B-planes in order to account for the 1/3 and 2/3<11$\bar{2}$0> reflections in the <111>//<0001> diffraction patterns. However, two assumptions were made in constructing this model: 1) that alternate basal planes contain pure Ag and Al_2Ag, and 2) that the A-planes have the higher Ag concentration. These choices were not totally arbitrary, however, since the strong intensities of the 0001, l=odd reflections and the large difference in contrast among alternate basal planes in the previous high-resolution images indicate that there is a substantial chemical difference between the A and B-planes. Also, in the previous high-resolution images where the atomic positions appeared bright on a dark background (Fig. 4 for example), the A-planes in the precipitate were generally darker than the B-planes, probably because they have a higher Ag concentration which causes greater electron scattering. Both of these assumptions can be tested by comparing experimental high-resolution images of γ' precipitates and the precipitate/matrix interface along the faces, with calculated images under comparable specimen and microscope conditions, as described in the following sections.

3.5 Simulated Images of Precipitates and Precipitate/Matrix Interface in a <110>//<11$\bar{2}$0> Orientation

3.5.1 Determination of Optimum Defocus Conditions

Interpretation of a high-resolution image in terms of the atomic structure of the specimen requires a detailed knowledge of the CTF of the microscope and its relationship with the spatial frequencies of the specimen (Spence 1981). In this study, the CTF for the JEOL 200CX was determined using the programs developed by Kilaas (1984) and the input values specified in Sect. 2.4. Figure 15 shows the CTF over a range of objective lens defocus values, starting at the minimum contrast condition Δz_{mc} = -240 Å and continuing through Scherzer defocus Δz_{Sch} = -660 Å, the second pass band $\Delta z_{2nd\ pb}$ = -1290 Å, to Δz = -1460 Å and out to the third pass band $\Delta z_{3rd\ pb}$ = -1690 Å. The spatial frequencies of the first-order precipitate and matrix reflections are indicated on the horizontal axes. These frequencies include the 0001 precipitate reflection at about 0.21 $Å^{-1}$, and the 0002, 01$\bar{1}$0, and 01$\bar{1}$1 precipitate reflections and 111 and 200 matrix

reflections, which lie between 0.40 to 0.50 $\mathring{A}^{-1}$. Note that at Scherzer defocus in Fig. 15(b), only spatial frequencies out to about 0.40 $\mathring{A}^{-1}$ are transferred with $\sin\chi = -1$ by the objective lens, while spatial frequencies greater than this are either truncated as the CTF approaches zero at 0.42 $\mathring{A}^{-1}$, or are transferred 180° out of phase since $\sin\chi = 1$. Thus, Scherzer defocus does not represent the optimum objective lens setting for the spatial frequencies of this specimen. However, when $\Delta z = -1460$ $\mathring{A}^{-1}$ as in Fig. 15(e), all of the spatial frequencies of the specimen are imaged with roughly the same phase and amplitude by the objective lens. Thus, this defocus represents an optimum imaging condition for the specimen, although because $\sin\chi = 1$ for all of the frequencies, the bright-field image of a weak-phase object consists of bright atoms on a dark background, where the brightness of the atoms is related to the projected specimen potential.

3.5.2 Image Calculations for the Precipitate Structure in a <11$\bar{2}$0> Orientation

The main objective of this section is to examine simulated high-resolution images of the γ' crystal structure in order to determine how variations in Ag concentration on alternate basal planes in the precipitate affect the appearance of the precipitate images. This information will indicate if high-resolution TEM can be used to determine whether the A and B-planes in the precipitate contain essentially 100 and 33 at.% Ag, respectively, as assumed by the model in Fig. 14.

Figure 16 shows simulated high-resolution images of a γ' precipitate as a function of objective lens defocus for alternate basal planes which vary in composition from 66 at.% Ag each in Fig. 16(a), to 99 at.% Ag on the A-planes and 33 at.% Ag on the B-planes in Fig. 16(d), for a constant crystal thickness of 54.4 $\mathring{A}$. The precipitate structure which contains equal amounts of Ag on the A and B-planes in Fig. 16(a) can be readily distinguished from the structures that contain unequal amounts of Ag in Figs. 16(b-d), by the difference in image contrast at Gaussian defocus ($\Delta z_G = 0$ $\mathring{A}$) and the minimum contrast condition ($\Delta z_{mc} = -240$ $\mathring{A}$). In addition, examination of the remaining images shows that the contrast is the same for both the A and B-planes when they contain the same concentration of Ag, regardless of the objective lens defocus. However, when the A and B-planes contain different amounts of Ag, as in Figs. 16(b-d), the image contrast is different for these two planes at all of the defocus values shown. Further, the difference in contrast between the A and B-planes often increases as the difference in Ag concentration between these planes increases, as demonstrated by comparing Figs. 16(b-d) at -1290 $\mathring{A}$ defocus, although this effect does not occur for all values of objective lens defocus. Thus, these simulations indicate that for certain defocus values it is possible to distinguish

between a precipitate which contains the same concentration of Ag on the A and B-planes from one that does not, and that it may also be possible to estimate the difference in Ag concentration between alternate basal planes in the precipitate by comparing the image contrast between alternate basal planes and/or by examining the change in contrast as a function of objective lens defocus, for a constant sample thickness.

Figure 17 shows a similar series of calculated images which demonstrates the change in image contrast between alternate basal planes with Ag concentration and specimen thickness for a constant objective lens defocus of -1460 Å. Again, the contrast between the A and B-planes does not change with specimen thickness when these planes contain the same concentration of Ag as in Fig. 17(a), but the contrast does change when the concentrations on these planes differ as in Figs. 17(b-d), provided that the specimen thickness is greater than about 20 Å. In addition, there is a similar progression in the appearance of the images with increasing thickness for the three structures in Figs. 17(b-d). For example, at 37.2 Å thickness the Ag-rich, A-planes are darker than the Al-rich, B-planes for all three models, while at 71.6 Å thickness the Ag-rich, A-planes are brighter than the Al-rich, B-planes. In fact, this reversal in contrast between the A and B-planes can make it impossible to distinguish between them just by examining the h.c.p. precipitate structure alone. That is, it is not possible to distinguish Fig. 17(c) at 71.6 Å thickness from Fig. 17(d) at 37.2 Å thickness, without previous knowledge of the positions of the A and B-planes. However, note that in both Figs. 17(c) and (d) at 54.4 Å thickness and in Fig. 17(b) at 37.2 Å thickness, translating from an atom position in an A-plane to an atom position in a B-plane involves moving from a relatively dark atom position to a brighter one. That is, atoms in the Al-rich, B-planes lie one-third of the lattice spacing (a/12<112>) to the right of the A atom positions in the plane below, and are brighter in these images at -1460 Å defocus. Also note that if any of these images are rotated by 180° such that the tops and bottoms of the figures are inverted, the opposite effect occurs. That is, translating from what appears to be an atom in an A-plane to an atom in a B-plane is accompanied by a decrease in the brightness of the atom positions. Thus, these simulated images indicate that the exact structure of the precipitate cannot be determined just by examination of the image intensity. However, the following section will show that the structure can be uniquely defined if the relationship between the ABA stacking of the {0001} planes in the precipitate can be compared with the ABC stacking sequence of the {111} planes in the matrix.

The reversal in contrast which occurs between the A and B-planes as the specimen thickness increases can be explained by examining the amplitude and phase of the 0001 beam as a function

of crystal thickness, as shown in Figs. 18 through 20. Figure 18 shows how the amplitude of the 0001 beam changes with increasing specimen thickness, as a function of the difference in Ag concentration between the A and B-planes. Note that the amplitude of the 0001 beam is always zero when the A and B-planes contain equal amounts of Ag, thus explaining why the contrast of these planes is always the same regardless of the specimen thickness or objective lens defocus. However, when the Ag concentrations between these planes differs, the amplitude of the 0001 beam steadily increases with thickness up to 75 Å, and the magnitude of the increase is proportional to the difference in Ag concentration between the two planes. Since the amplitude of the 0001 beam increases with crystal thickness up to 75 Å, its effect on the image contrast should also increase with thickness. This does occur, as demonstrated by comparing Figs. 17(b-d) at 17.2 Å thickness where there is almost no evidence of the 0001 periodicity, with images at greater thicknesses where there is always a contrast difference between alternate basal planes. Figure 19 further shows the change in amplitude of the 0001 beam for a precipitate which contains 99 at.% Ag on the A-planes and 33 at.% Ag on the B-planes up to a crystal thickness of 200 Å and also, the amplitudes of the other first-order precipitate reflections which are used to form the high-resolution images in this study.

Figure 20 shows the variation in phase of the first-order beams with crystal thickness up to 200 Å. Due to the high scattering power of Ag, the phases of most beams vary significantly from $-\pi/2$ at a thickness of only 50 Å, indicating that the weak-phase object approximation is only valid for γ' precipitates which are less than about 20 Å thick. In addition, the phase of the 0001 beam changes by almost 2π by the time the crystal has reached a thickness of only about 70 Å, while the phase of the 0002 beam is roughly constant up to this thickness. This explains the contrast reversal which occurs between the A and B-planes up to this thickness. The phase of the 0001 beam changes from about $\pi/2$ at 35 Å to $-\pi/2$ at 70 Å, while the relative amplitudes of the 0001 and 0002 beams and the phase of the 0002 beam remain nearly constant at these thicknesses.

Thus, the results from the simulated images examined in Figs. 16 and 17 indicate that it may be possible to determine whether the A and B-planes in the γ' precipitates contain about 100 and 33 at.% Ag, respectively, as proposed for the model in Fig. 14, but only for certain combinations of objective lens defocus and specimen thickness, and provided that the correspondence between the atomic stacking in the precipitate and matrix can be determined. While it is possible to determine the objective lens defocus to the accuracy needed for correct image interpretation by optical diffraction, it is difficult to measure the specimen thickness in the thin areas where high-

resolution images are most easily interpreted. As was demonstrated by Fig. 17, this can represent a serious problem for distinguishing between the A and B-planes in the precipitate when one of the planes is dark. In this case, the only way to make this distinction is to examine the precipitate image over a gradation in specimen thickness near the edge of the hole, which either causes the atoms in both planes of the precipitate to appear at some thickness, or produces sufficient detail in the image at the precipitate/matrix interface that the A and B-planes can be distinguished by their relation with the matrix.

3.5.3 Image Simulations of the Precipitate/Matrix Interface in a <110>//<11$\bar{2}$0> Orientation

Figure 21 shows a series of calculated images for a γ' precipitate/matrix interface in a <110>//<11$\bar{2}$0> orientation, as a function of both specimen thickness and objective lens defocus. The model for this interface is shown by the projected potential in the top-left corner of Fig. 21. In this model, the A-planes in the precipitate contain pure Ag while the B-planes contain 33 at.% Ag, as for the model γ' precipitate crystal in Fig. 14. The precipitate/matrix interface is between the last Ag-rich, A-plane in the precipitate and the first B-plane in the Al matrix. By examining the images in Fig. 21, it is apparent that for certain values of objective lens defocus and specimen thickness, such as at -1460 Å defocus and 37.2 Å thickness, it is possible to determine the atomic structure of both the precipitate and precipitate/matrix interface, since there is just enough contrast in the dark precipitate planes to determine the atom positions. For example, examination of the precipitate structure in this image shows that moving from an atom position in a dark plane to a bright atom position in the plane above, requires a translation of a/12<112> to the right. Since this translation is needed to move from an atom position in an A-plane to one in a B-plane, it can tentatively be decided that the A-plane is Ag-rich. However, as mentioned in the previous section, positive confirmation of the A and B-planes requires that the ABA stacking sequence in the precipitate progress in the same direction as the ABC stacking sequence in the matrix. Further examination of the matrix in this image shows that stacking of the A, B and C-planes occurs by translation of the atoms a/12<112> to the right, thus verifying that the A and B-planes in the precipitate were correctly chosen and therefore, that the A-planes are Ag-rich. If a contrast reversal had occurred between the A and B-planes in the precipitate, moving from a dark atom position to a bright one would have required a translation of a/12<112> to the left, which is opposite to the translation in the matrix. Lastly, it should be mentioned that a number of additional image simulations, which examined the image contrast of the precipitate as a function of both crystal and beam tilt were also performed, and these results are reported elsewhere (Howe and Gronsky 1986b).

3.6 Comparison Between Calculated and Experimental High-Resolution Images of the Precipitate/Matrix Interface

Figure 22 shows an experimental high-resolution TEM image of a γ' precipitate/matrix interface in a $\langle 110\rangle//\langle 11\bar{2}0\rangle$ orientation. The amorphous layer at the edge of the foil is just visible in the left side of this figure, and the corresponding electron and optical diffraction patterns are also shown in the upper-left and right corners, respectively. Comparing the spatial frequencies of the specimen and halos in the optical diffraction pattern in Fig. 22 with the contrast transfer functions in Fig. 15, indicates that this image was taken at about -1440 Å defocus. In addition, examination of the high-resolution image shows that the brightness of the atoms in the darker planes of the precipitate slowly decreases from left to right in the micrograph. Comparing this contrast change with the simulated images in Fig. 21 shows that good agreement is obtained for a sample thickness that varies from about 20 Å at the edge to about 40 Å on the right side of the micrograph. This is illustrated by the inset smulated image of the interface at -1440 Å defocus and 37.2 Å thickness, taken from Fig. 21. Thus, because this micrograph satisfies the conditions needed for correct interpretation of an experimental image previously discussed, it is possible to conclude that the model for the precipitate/matrix interface in Fig. 21 is correct. This further implies that the model for the γ' precipitate in Fig. 14 is also correct, since this model was used to construct the h.c.p. part of the interface. The precipitate structure can be further confirmed by comparing the brightness of the atoms on alternate basal planes with the stacking sequences in both the precipitate and matrix in Fig. 22. In this case, moving from an A-plane to a B-plane involves a translation of $a/12\langle 112\rangle$ to the right, and is accompanied by an increase in brightness of the atoms in the B-planes. As discussed in the previous section, this information is sufficient to conclude that the A-planes are Ag-rich and that the B-planes are Al-rich.

The only factor in the model in Fig. 14 that cannot be completely determined from this micrograph, is the concentration of Ag in the A and B-planes of the precipitate. However, it is possible to conclude that the A and B-planes contain at least a 40 at.% difference in Ag concentration, because the atoms are almost invisible at about 40 Å thickness in Fig. 22, which only occurs for precipitate structures that contain at least 88 at.% Ag on the A-planes, as is demonstrated by comparing Figs. 17(b-d) at 37.2 Å.

Figure 23(a) shows a second high-resolution image of a precipitate/matrix interface from a different thin foil. The corresponding electron diffraction pattern is shown in Fig. 23(b), and an optical diffraction pattern, which mainly contained the area enclosed in Fig. 23(a), is shown in Fig. 23(c). Note that all of the first-order precipitate and matrix periodicities are present in the

optical diffraction pattern from the interface. This image was taken at about -1460 Å defocus, as determined from the amorphous edge of the sample, which is off the left side of the micrograph. Although one set of basal planes is almost entirely out of contrast in the micrograph, there are a few atoms which are visible in these planes, as indicated by arrows in Fig. 23(a). By comparing these atom positions with those in the bright atom planes, it is possible to determine that the ABA stacking sequence in the precipitate proceeds by an a/12<112> translation to the right, from an atom in a dark A-plane to an atom in a bright B-plane above, and that this same translation is observed in the matrix. Thus, it is again possible to conclude that the A-planes in the precipitate are Ag-rich. This is further demonstrated in Fig. 24, where the area enclosed in Fig. 23(a) is shown enlarged in Fig. 24(c), and compared with the projected potential for a precipitate, which has pure Ag on the A-planes and 33 at.% Ag on the B-planes in Fig 24(a), and an image calculated from this projected potential at 40.1 Å thickness and -1460 Å defocus in Fig. 24(b). There is excellent agreement between the calculated and experimental images in this figure, and judging from the low contrast of the A-planes in the precipitate in Fig. 24(c), it is possible to conclude that these planes are nearly pure Ag, further supporting the model γ' structure in Fig. 14.

3.7 Atomic Mechanisms of Precipitate Plate Growth

Since the structure and chemistry of γ' precipitates and the precipitate/matrix interface have been determined at the atomic level, it is possible to further establish the relationship between the structural and chemical components of the transformation, enabling growth of the γ' precipitates to be described at the atomic level. Figure 25 shows an enlargement of the projected potential previously discussed in Fig. 21. The γ' precipitate in this model is composed of A-planes that are pure Ag and B-planes that contain 33 at.% Ag. The stacking sequences in both the precipitate and matrix are also labelled, and the precipitate/matrix interface is indicated by a solid line. In order for the precipitate to thicken, two processes must occur: 1) a Shockley partial dislocation must propagate along the C-plane in the matrix and translate these atoms into A-positions, and 2) there must be a corresponding chemical change which allows the A-planes in the precipitate to contain pure Ag and the B-planes to contain 33 at.% Ag. Thus, both the structural and major chemical changes which are necessary for growth of the precipitate occur in the same atom plane. In addition, since it was previously shown that both the thickening and lengthening of γ' precipitate plates appear to occur by the movement of kinks in Shockley partial dislocation ledges, it is possible to further infer that growth of the γ' precipitates occurs by the substitutional diffusion of Ag atoms across kinks in the Shockley partial dislocation ledges, and that this is the limiting

reaction in the growth process. Thus, by combining the information available from high-resolution TEM, image simulations, CBED and EDS, it is possible to describe the mechanisms of the transformation at the atomic level.

It is also apparent from Fig. 25, that the B-plane in the two-plane ledge does not undergo a structural transformation as the Shockley partial dislocation propagates along the interface. Consequently, substitutional diffusion of Ag within this plane across the ledge is roughly independent of the ledge structure, indicating that structural aspects of the transformation such as the disorder associated with kinks and their density along the ledge mainly need to be considered for only the upper-atom plane in a two-plane ledge. In addition, because the B-plane possesses the required structural arrangement for the h.c.p. precipitate before the Shockley partial dislocation passes along the interface, significant compositional changes may occur in this plane prior to its incorporation into the precipitate. Thus, while previous kinetic analyses have been highly successful in predicting the growth rates of both the edges and ledges on the faces of precipitate plates by assuming that they are disordered interfaces (Trivedi 1982, Laird and Aaronson 1969, Ferrante and Doherty 1976), the observations in this study indicate that the growth interfaces are almost entirley coherent and therefore, that the structural aspects of the transformation need to be taken into account in order to understand and accurately model the growth process on an atomic level.

There are several possible reasons why the Ag atoms only join the γ' precipitates at kinks in the Shockley partial dislocation ledges. First, atomic models (Howe et al. 1985a) indicate that introduction of a kink into a Shockley partial dislocation ledge produces a distortion, that leads to an open space at the precipitate/matrix interface, as illustrated in Fig. 26. This excess volume at the kink should reduce the activation energy for migration of a solute atom across the interface, in the same way that the activation energy is reduced for migration of an atom along a grain boundary (Smith, Rae and Grovenor 1980). Secondly, if an atom is incorporated into the h.c.p. precipitate by the movement of a kink parallel to the dislocation line direction, both the dislocation line length and the number of unlike bonds across the precipitate/matrix interface remain constant while the interface advances, an energetically favorable situation. Thirdly, atoms which approach the Shockley partial dislocation and cross the interface at kinks only have to perform partial jumps close to the interface (Dahmen 1986), which should facilitate migration toward the ledge and rapid transfer across the kink. Thus, energetic considerations suggest several reasons why the Ag atoms only cross the pecipitate/matrix interface at kinks in the Shockley partial dislocations which accomplish the f.c.c. $\rightarrow$ h.c.p. structural transformation.

4. CONCLUSIONS

The purpose of the present research was to perform highly detailed analyses of both the structural and chemical components required for growth of γ' plate-shaped precipitates in an Al-Ag alloy, in order to understand the mechanisms of precipitate growth at the atomic level. In order to accomplish this, the techniques of high-resolution TEM and image simulations, EDS microanalysis and CBED were employed. The major findings of this study are: **1)** comparison between experimental and simulated high-resolution TEM images of Shockley partial dislocation ledges shows that both the faces and edges of γ' precipitate plates grow by the passage of Shockley partial dislocations along alternate {111} matrix planes, **2)** the elastic strain energy associated with the f.c.c. → h.c.p. structural transformation is minimized by the nucleation of equal numbers of all three variants of Shockley partial dislocations on the same {111} faces of precipitates, **3)** all interfaces of γ' precipitates are largely coherent and faceted along low-energy $\langle 111 \rangle // \langle 0001 \rangle$ and $\langle 110 \rangle // \langle 11\bar{2}0 \rangle$ directions at the atomic level, thereby minimizing both the chemical and structural interfacial energies associated with the interphase boundary, **4)** the composition of the γ' precipitates is approximately Ag_2Al, and the precipitates possess long-range order on alternate basal planes during the early stages of growth at 350 °C, where the A-planes in the precipitates contain nearly pure Ag and the B-planes have the composition Al_2Ag, and **5)** agreement between experimental and calculated high-resolution TEM images of the precipitate/matrix interface indicates that the limiting reaction in the growth process is the substitutional diffusion of Ag atoms across kinks in the Shockley partial dislocations ledges, which terminate in the Ag-rich, A-planes of the precipitate.

5. ACKNOWLEDGEMENTS

This research was supported by the Director, Office of Energy Research, Office of Basic Energy Sciences, Materials Science Division of the U.S. Department of Energy under Contract No. DE-AC03-76SF00098.

6. REFERENCES

Aaronson H.I., 1962, in *Decomposition of Austenite by Diffusional Processes*, Interscience Pub., New York, 387.

Aaronson H.I., Laird C. and Kinsman K.R., 1970, in *Phase Transformations*, ASM, Metals Park, OH, 313.

Aaronson H.I., 1974, *J. Microscopy*, **102(3)**, 275.

Aaronson H.I., 1977, *Scripta Met.*, **11**, 731.

Aaronson H.I., Lee J.K. and Russell, K.C., 1977, in *Precipitation Processes in Solids*, TMS-AIME, Warrendale, PA, 31.

Aaronson H.I., 1979, *Trans. Indian Inst. Metals*, **32(1)**, 1.

Alexander K.B., LeGoues F.K., Laughlin D.E. and Aaronson H.I., 1984, *Acta Met.*, **32**, 2241.

Atkinson C., 1982, Proc. Roy. Soc. London, **A384**. 167.

Burton W.K., Cabrera N. and Frank F.C., 1950-51, *Phil. Trans. Roy. Soc.*, **A243**, 299.

Chen Y.H. and Doherty R.D., 1977, *Scripta Met.*, **11**, 725.

Christian J.W., 1965, *The Theory of Transformations in Metals and Alloys*, Pergamon Press, Oxford, 449.

Cliff G. and Lorimer G.W., 1975, *J. Microscopy*, **110**, 107.

Dahmen U., 1986, submitted to *Scripta Met.*

Dahmen U. and Westmacott K., 1983a, *Phys. Stat. Sol. (a)*, **80**, 249.

Dahmen U. and Westmacott K., 1983b, *Scripta Met.*, **17**, 1241.

Ferrante M. and Doherty R.D., 1976, *Scripta Met.*, **10**, 1059.

Frank F.C., 1951, *Phil. Mag.*, **42**, 809.

Gjonnes J. and Moodie A.F., 1965, *Acta Cryst.*, **19**, 65.

Goldstein J.I., 1979, in *Introduction to Analytical Electron Microscopy*, Plenum Press, New York, 86.

Hirsch Sir P., Howie A., Nicholson R.B., Pashley D.W. and Whelan M.J., 1979, *Electron Microscopy of Thin Crystals*, Robert E. Krieger, Pub., Malabar, FL, 261.

Hirth J.P. and Lothe J., 1960, *Theory of Dislocations*, McGraw-Hill Co., New York, 144.

Howe J.M., Aaronson H.I. and Gronsky R., 1985a, *Acta Met.*, **33(4)**, 639.

Howe J.M., Aaronson H.I. and Gronsky R., 1985b, *Acta Met.*, **33(4)**, 649.

Howe J.M. and Gronsky R., 1985, *Ultramicroscopy*, **18**, 83.

Howe J.M. and Gronsky R., 1986a, submitted to *Scripta Met.*

Howe J.M. and Gronsky R., 1986b, to be submitted to *Ultramicroscopy*.

Howe J.M., Sarikaya M. and Gronsky R., 1986, *Acta Cryst.*, in press.

Howe J.M., 1985, *Ph.D. Thesis*, University of California, Berkeley, CA.

Hren J.A. and Thomas G., 1963, *TMS-AIME*, **227**, 308.

Jones G.J. and Trivedi R., 1975, J. Crystal Growth, **29**, 155.

Kilaas R., 1984, *unpublished research.*

Laird C. and Aaronson H.I., 1967, *Acta Met.*, **15**, 73.

Laird C. and Aaronson H.I., 1969, *Acta Met.*, **17**, 505.

Mondolfo L.F., 1979, *Aluminum Alloys: Structure and Properties*, Butterworths, London, 213.

Nicholson R.B. and Nutting J., 1961, *Acta Met.*, **9**, 332.

Neumann J.P., 1966, *Acta Met.*, **14**, 505.

O'Keefe M.A. and Buseck P.R., 1979, *Trans. Amer. Cryst. Assoc.*, **15**, 27.

Rajab K.E. and Doherty R.D., 1982, in *Proceedings of an International Conference on Solid → Solid Phase Transformations*, TMS-AIME, Warrendale, PA, 555.

Reynolds, Jr. W.T., Enomoto M. and Aaronson H.I., 1984, in *Phase Transformations in Ferrous Alloys*, TMS-AIME, Warrendale, PA, 155.

Rosenberg A. and Tiller W.A., 1957, *Acta Met.*, **5**, 565.

Sagoe-Crentsil K.K. and Brown L.C., 1984, *Met. Trans.*, **15A**, 1969.

Sarikaya M. and Thomas G., 1984, in *Analytical Electron Microscopy*, San Francisco Press, San Francisco, CA, 97.

Shewmon P.G., 1969, *Transformations in Metals*, McGraw-Hill Co., New York, 274.

Smith D.A., Rae C.M.F. and Grovenor C.R.M., 1980, in *Grain Boundary Structure and Kinetics*, ASM, Metals Park, OH, 337.

Smith D.J., Bursill L.A. and Wood G.J., 1985, *Ultramicroscopy*, **1**, 19.

Spence J.C.H., 1980, *Notes Accompanying the A.S.U. Multisice Programs.*

Spence J.C.H., 1981, *Experimental High-Resolution Electron Microscopy*, Clarendon Press, Oxford, 356.

Thompson N., 1953, *Proc. Phys. Soc.*, **66B**, 481.

Trivedi R., 1982, in *Proceedings of a International Conference on Solid → Solid Phase Transformations*, TMS-AIME, Warrendale, PA, 477.

7. FIGURE CAPTIONS

Figure 1. (a) and (b) Projected potentials for single 90° and 30° Shockley partial dislocation ledges on the face of a γ' precipitate, respectively, (c) and (d) corresponding simulated high-resolution TEM images for a foil thickness of 34.4 Å and an objective lens defocus of -1460 Å, and (e) and (f) simulated images for a foil thickness of 71.6 Å and an objective lens defocus of -1460 Å. The dislocation cores are circled and the stacking sequences on both sides of the ledges are indicated in the projected potentials.

Figure 2. (a) and (c) Burgers circuit that can be used to distinguish a 90° Shockley partial dislocation, and (b) and (d) Burgers circuit that distinguishes a 30° Shockley partial dislocation. S_e and S_s indicate the start of the 90° (edge) and 30° (screw) Burgers circuits, respectively, while F indicates the finish of the circuits.

Figure 3. Bright-field TEM micrograph illustrating the lengths and thicknesses of γ' precipitates produced by aging the Al-4.2 at.% Ag alloy for 30 min. at 350°C. The foil normal is $\langle 110 \rangle_{Al}$.

Figure 4. Experimental $\langle 110 \rangle // \langle 11\bar{2}0 \rangle$ high-resolution TEM image of an approximately ten-plane ledge on the face of a γ' precipitate, with a Burgers circuit that indicates the presence of four 30° Shockley partial dislocations associated with the ledge.

Figure 5. High-resolution image of a γ' precipitate edge in a $\langle 110 \rangle // \langle 11\bar{2}0 \rangle$ orientation at -1690 Å defocus. A 2:1 ratio of 30° to 90° Shockley partial dislocations at the edge is revealed by the two types of Burgers circuits described in Fig. 2.

Figure 6. Illustration of two different ways of transforming cubic close-packed planes into hexagonal close-packed planes: (a) using the same Shockley partial dislocation on alternate (111) planes, and (b) using equal numbers of all three types of Shockley partial dislocations on alternate (111) planes. Each block represents two (111) matrix planes (after Shewmon 1969).

Figure 7. (a) $\langle 111 \rangle // \langle 0001 \rangle$ selected-area diffraction pattern containing both precipitate and matrix reflections as indicated, (b) diffraction conditions used to obtain axial high-resolution images of the precipitate, and (c) tilted-illumination conditions used to resolve the 1.4 Å spacing of the {220} matrix and $\{11\bar{2}0\}$ precipitate planes.

Figure 8. Crystallographic features of a γ' plate oriented perpendicular to the electron beam.

The six edges which parallel <110> directions within the (111) matrix plane are numbered, and facets on the edges which parallel <112> directions are indicated by arrows.

Figure 9. (a) Low-magnification axial image of facets on the edge of a precipitate plate. Comparison with the matrix directions shown in the figure indicates that the precipitate/matrix interface parallels a $[\bar{1}\bar{1}2]$ direction overall, but that the facets closely follow <110> directions on a nearly atomic level. (b) Enlargement from region A in Fig. 9(a) showing single-atom facets along <110> at the precipitate edge. The foil normal is <111>//<0001>.

Figure 10. A <111>//<0001> tilted-illumination, high-resolution image at the corner of a γ' precipitate. The 1.4 Å {220} matrix planes are continuous as they cross the interphase boundary to become the $\{11\bar{2}0\}$ precipitate planes, demonstrating that the precipitate/matrix interface is coherent in this orientation.

Figure 11. (a) A second tilted-illumination image which shows a series of single-atom ledges migrating along the precipitate edge. The ledges (arrows) are diffuse while the terraces between the ledges are atomically flat along the <110> direction. Foil normal is <111>//<0001>. (b) Atomically smooth solid/solid interface with atoms represented by cubes, illustrating the terrace-ledge-kink mechanism of growth.

Figure 12. (a) Bright-field TEM image of micron-sized extracted precipitates on a carbon film, (b) EDS spectrum from the precipitate with the Al Kα and Ag Kα peaks indicated, and (c) and (d) enlargements of the Al Kα and Ag Kα peaks. The large Cu peak in (b) is due to fluorescence from the supporting Cu grid.

Figure 13. (a) and (b) Two <110>//$<11\bar{2}0>$ CBED patterns from γ' precipitates located a short distance apart in the same thin foil. The 000l, l=odd precipitate reflections in (a) display strong, uniform intensities indicating that they are allowed, while the same reflections in (b) contain G-M lines indicating that they are forbidden.

Figure 14. Atomic model for γ' precipitates. The A-planes in the precipitate are pure Ag and the B-planes are Al_2Ag, producing an average precipitate composition of Ag_2Al. Each Ag atom in the B-planes is also surrounded by six Al atoms, and the Ag atoms can occupy any of the three positions shown in the B-plane.

Figure 15. (a-f) CTF for the JEOL 200CX over a range of objective lens defocus values, with C_s = 1.2 mm, Δ = 50 Å, α_i = 1.0 mrad, Acc. Volt. = 200 keV, and Δz_{Sch} = -660 Å.

Figure 16. (a) Simulated high-resolution TEM images of a γ' precipitate containing 66 at.% Ag on both the A and B-planes for a range of objective lens defocus values and a thickness of 54.4 Å, and (b-d) similar images for precipitates in which the Ag concentration in the A-planes increases by 10 at.% Ag and that in the B-planes decreases by the same amount until 99 at.% Ag in the A-planes and 33 at.% Ag in the B-planes is achieved.

Figure 17. (a-d) A series of simulated images which demonstrates the change in image contrast that occurs between A and B-planes as a function of Ag concentration and crystal thickness, for an objective lens defocus of -1460 Å.

Figure 18. Amplitude of the 0001 reflection for a precipitate with an average composition of 66 at.% Ag, as a function of the difference in Ag concentration between alternate basal planes and increasing thickness.

Figure 19. Amplitudes of the forward-scattered beam and the first-order precipitate reflections as a function of crystal thickness, for a γ' precipitate which contains 99 at.% Ag on the A-planes and 33 at.% Ag on the B-planes. The amplitudes were normalized by dividing by the sum of the amplitudes.

Figure 20. Phases of the forward-scattered beam and the first-order, Bragg-scattered beams in Fig. 19 as a function of crystal thickness, for a γ' precipitate with 99 at.% Ag on the A-planes and 33 at.% Ag on the B-planes. The phases of the Bragg-scattered beams were normalized by subtracting the phase of the forward-scattered beam.

Figure 21. Simulated images of a γ' precipitate/matrix interface as a function of objective lens defocus and specimen thickness. The γ' precipitate contains pure Ag on the A-planes and 33 at.% Ag on the B-planes, and the interface is between the last Ag-rich, A-plane in the precipitate and the first B-plane in the Al matrix.

Figure 22. Experimental high-resolution TEM image of a γ' precipitate/matrix interface in a $\langle 110\rangle//\langle 11\bar{2}0\rangle$ orientation, with the corresponding electron and optical diffraction patterns. A matching simulated image of the interface at -1440 Å defocus and 37.2 Å thickness is superimposed on the experimental image.

Figure 23. (a) High-resolution image of a second precipitate/matrix interface at -1460 Å defocus, (b) electron diffraction condition for the image with the objective aperture position indicated, and (c) an optical diffraction pattern from the area enclosed in (a).

Figure 24. (a) Projected potential for the pecipitate/matrix interface with a γ' precipitate containing 99 at.% Ag on the A-planes and 33 at.% Ag on the B-planes, (b) corresponding simulated image for a crystal thickness of 40.1 Å and an objective lens defocus of -1460 Å, and (c) experimental image from the region enclosed in Fig. 23 (a).

Figure 25. Illustration showing how the structural and major chemical changes needed for growth of a γ' precipitate plate occur in the same atomic plane when the A-planes of the precipitate are Ag-rich and the Shockley partial dislocation propagates along the C-plane in the matrix.

Figure 26. Atomic model of a single-atom kink in a Shockley partial dislocation ledge lying along a <110> direction. The figure normal is <111> and atoms which occupy B-positions in the bottom plane of atoms and either A or C-positions in the top atom plane are distinguished at the top of the figure. Note the open space associated with the kink, outlined in the figure.

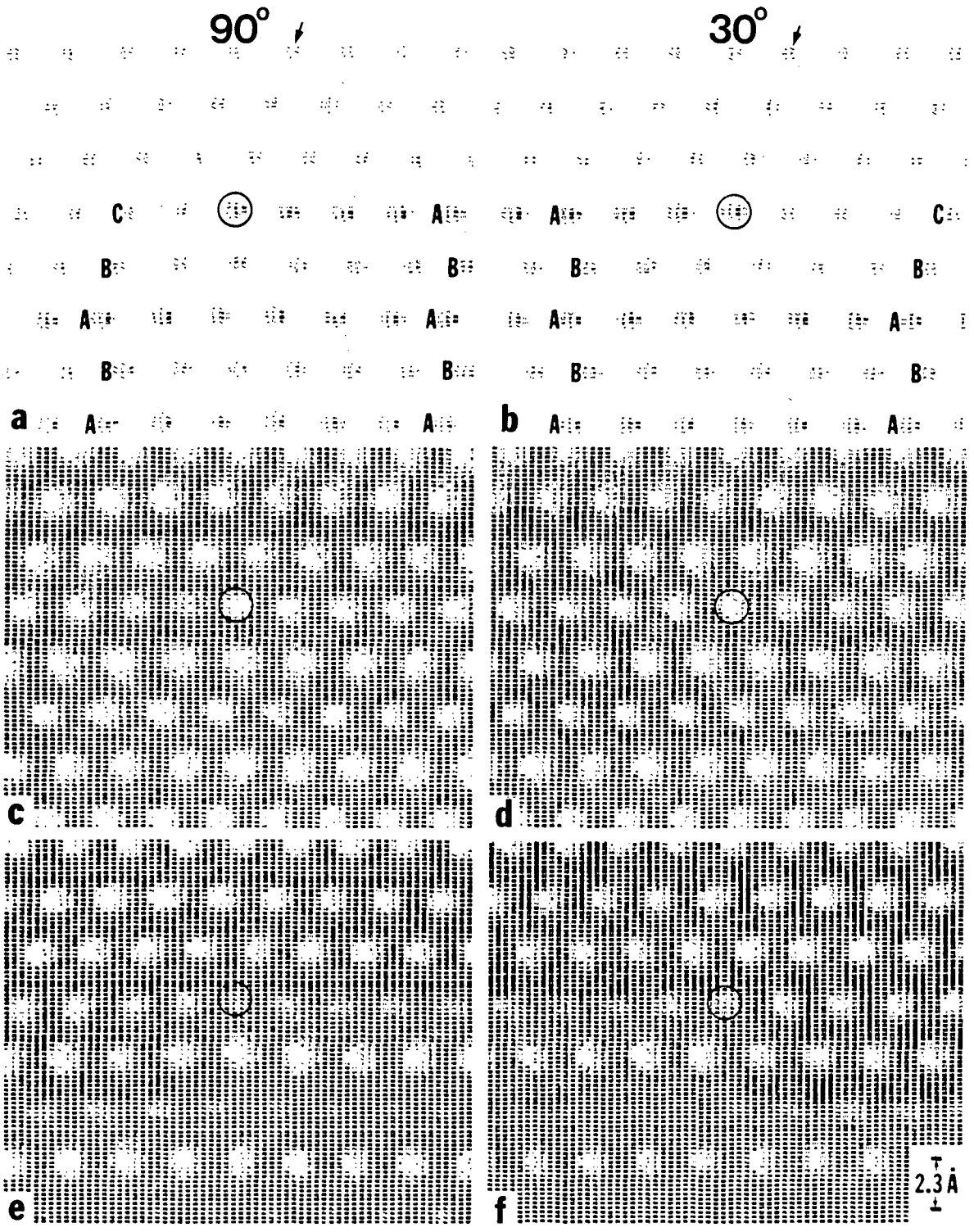

XBL 857-3141

Fig. 1

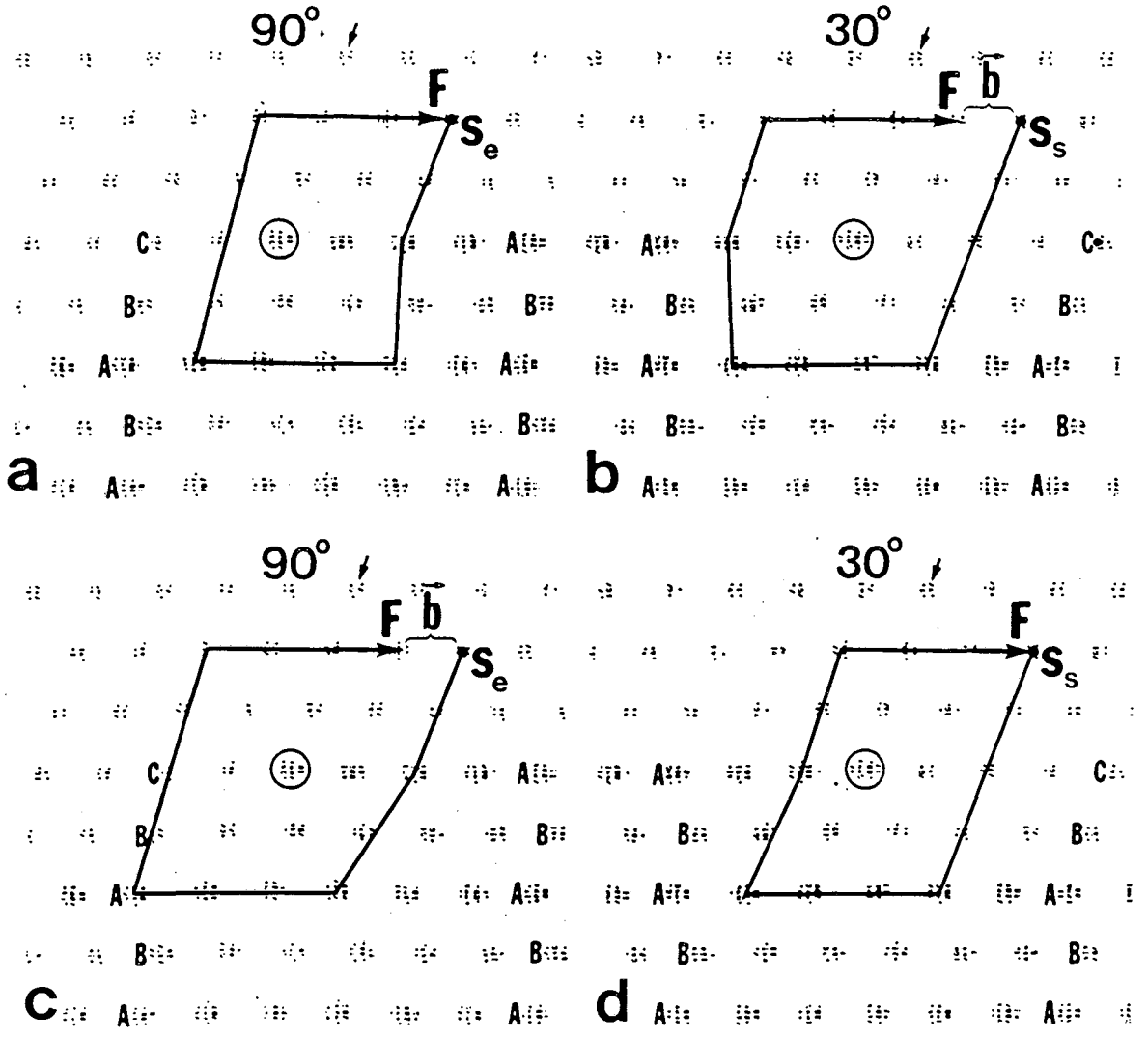

XBL 863-1062

Fig. 2

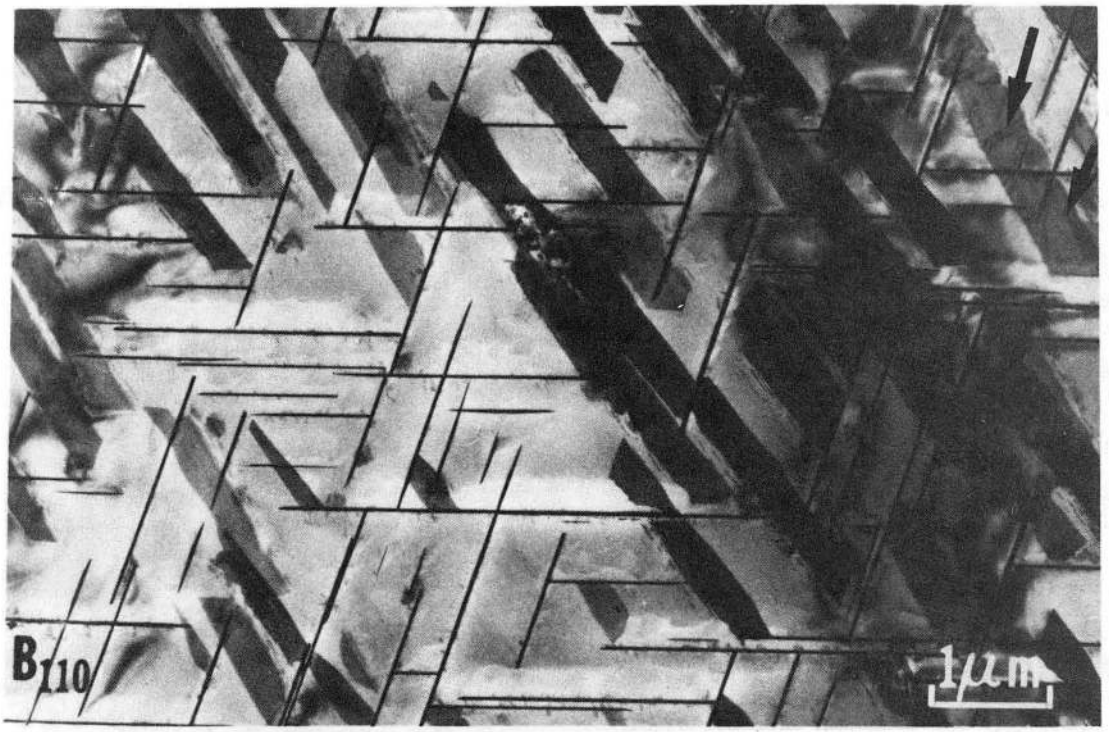

XBB 842-1207

Fig. 3

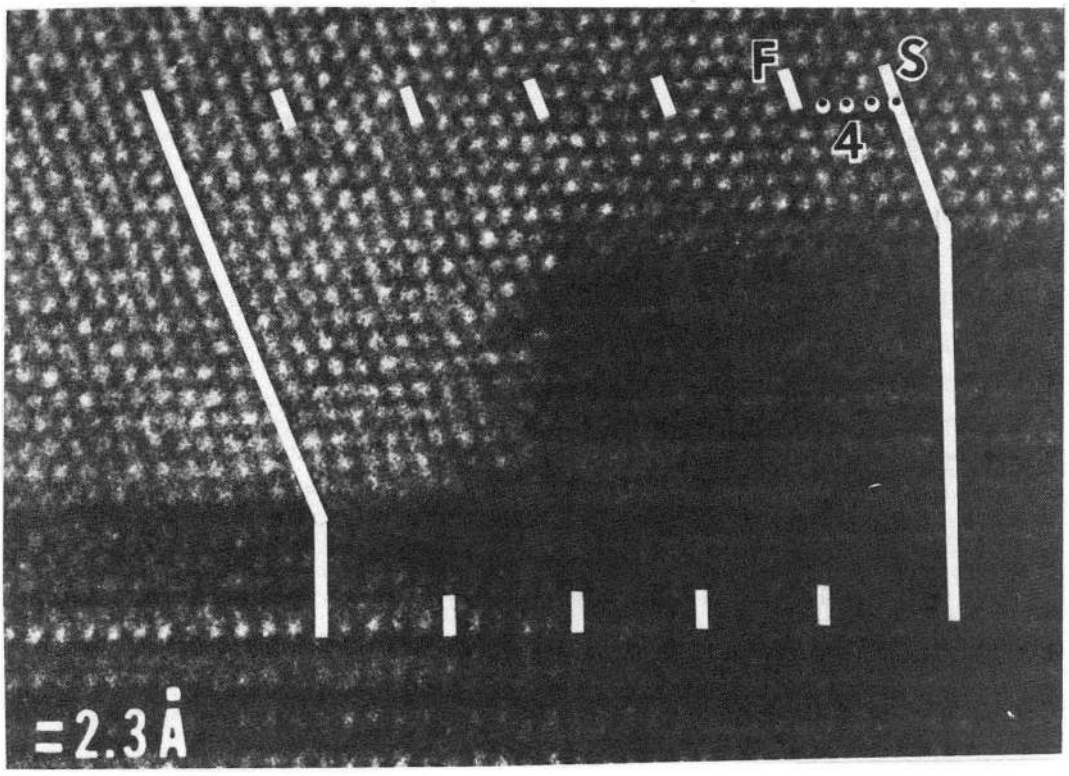

XBB 830-10305-B

Fig. 4

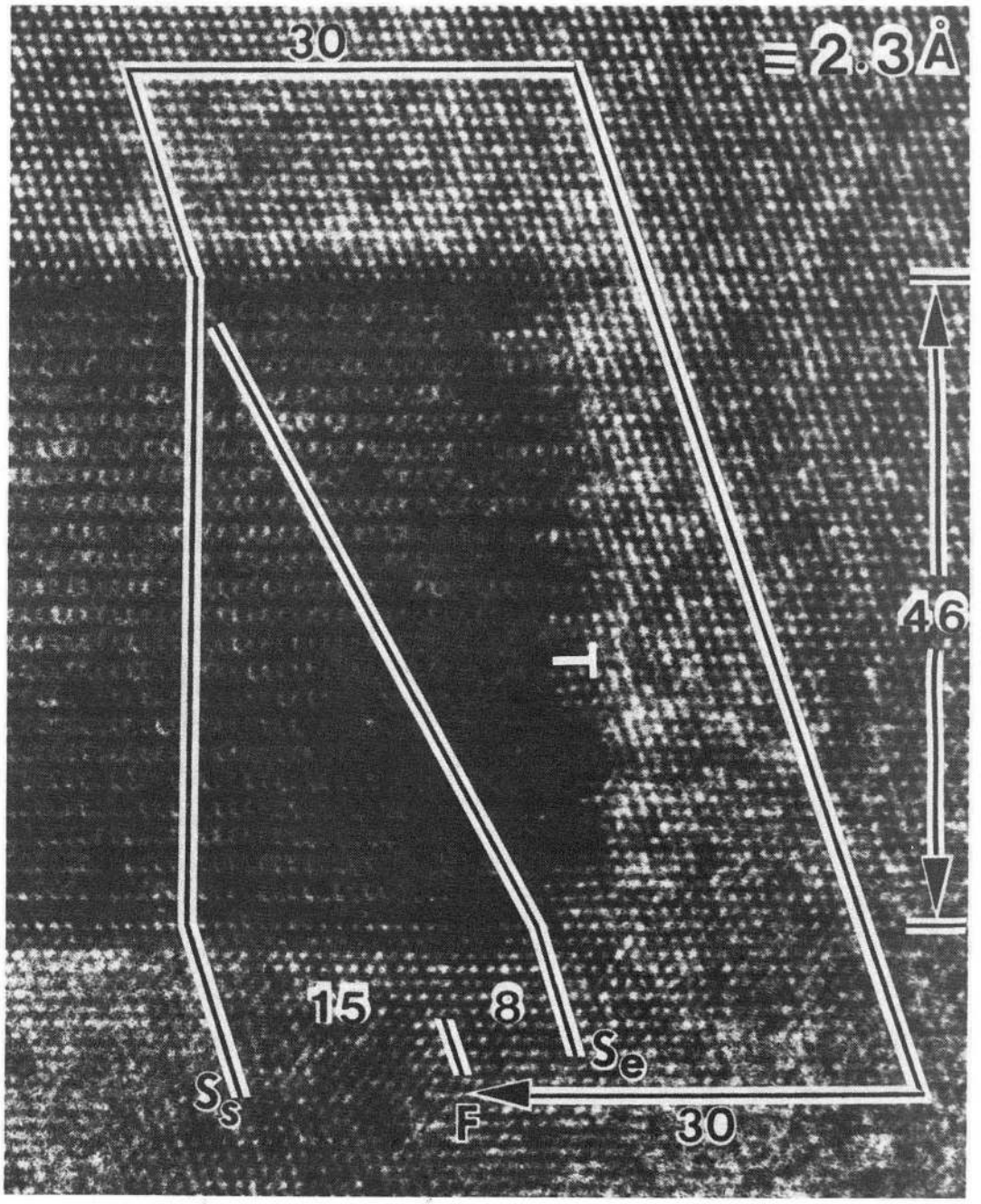

XBB 840-9360

Fig.5

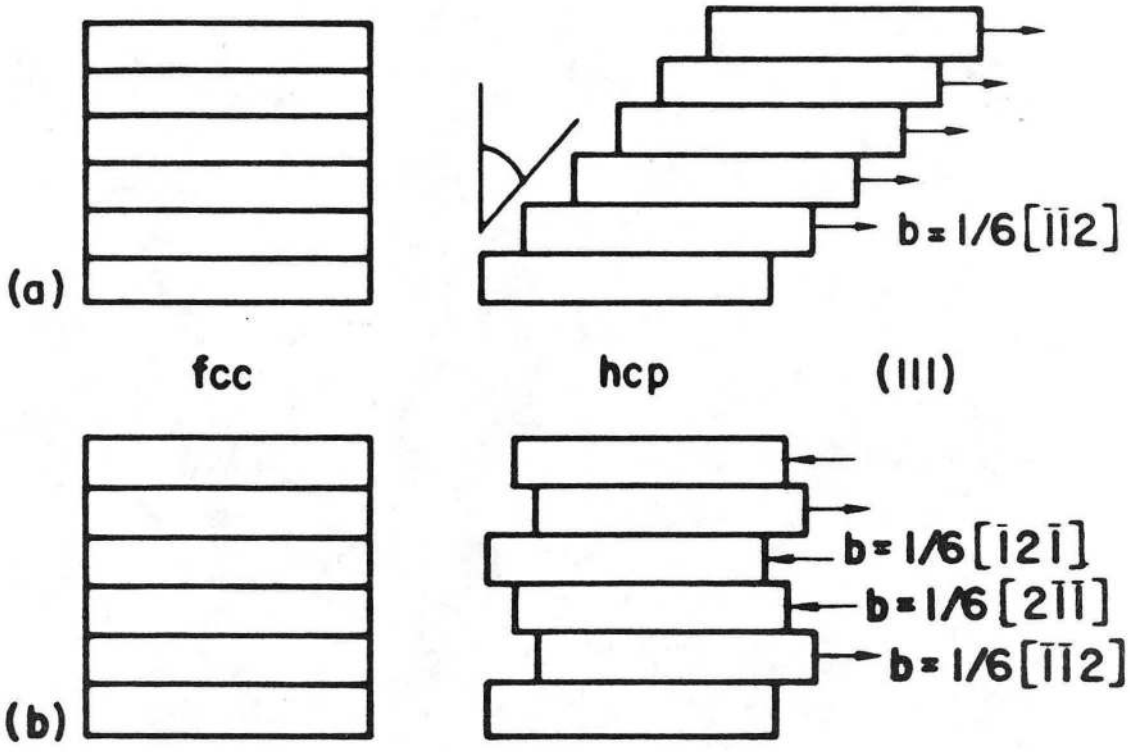

XBL 841-10016

Fig. 6

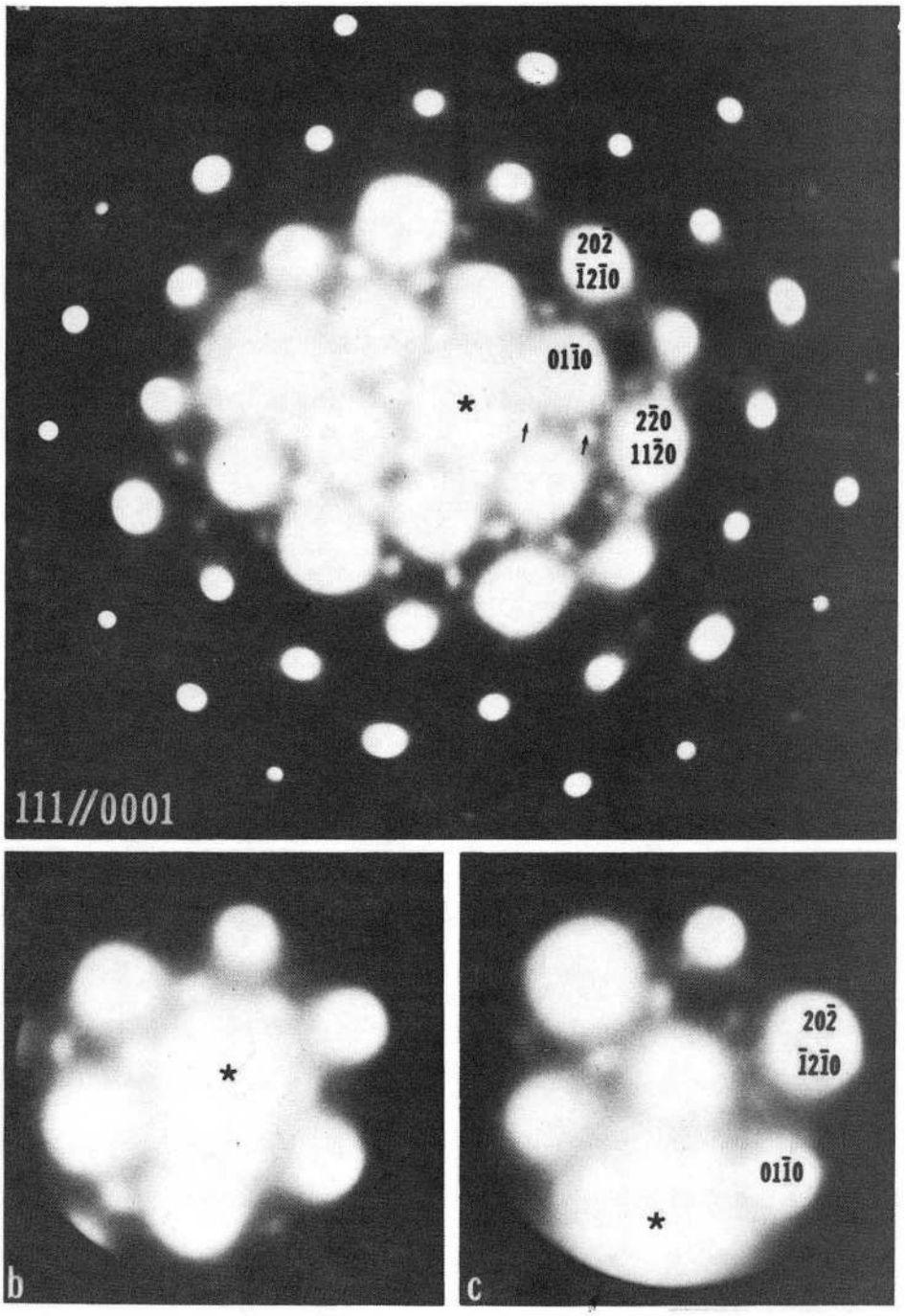

XBB 842-1227

Fig. 7

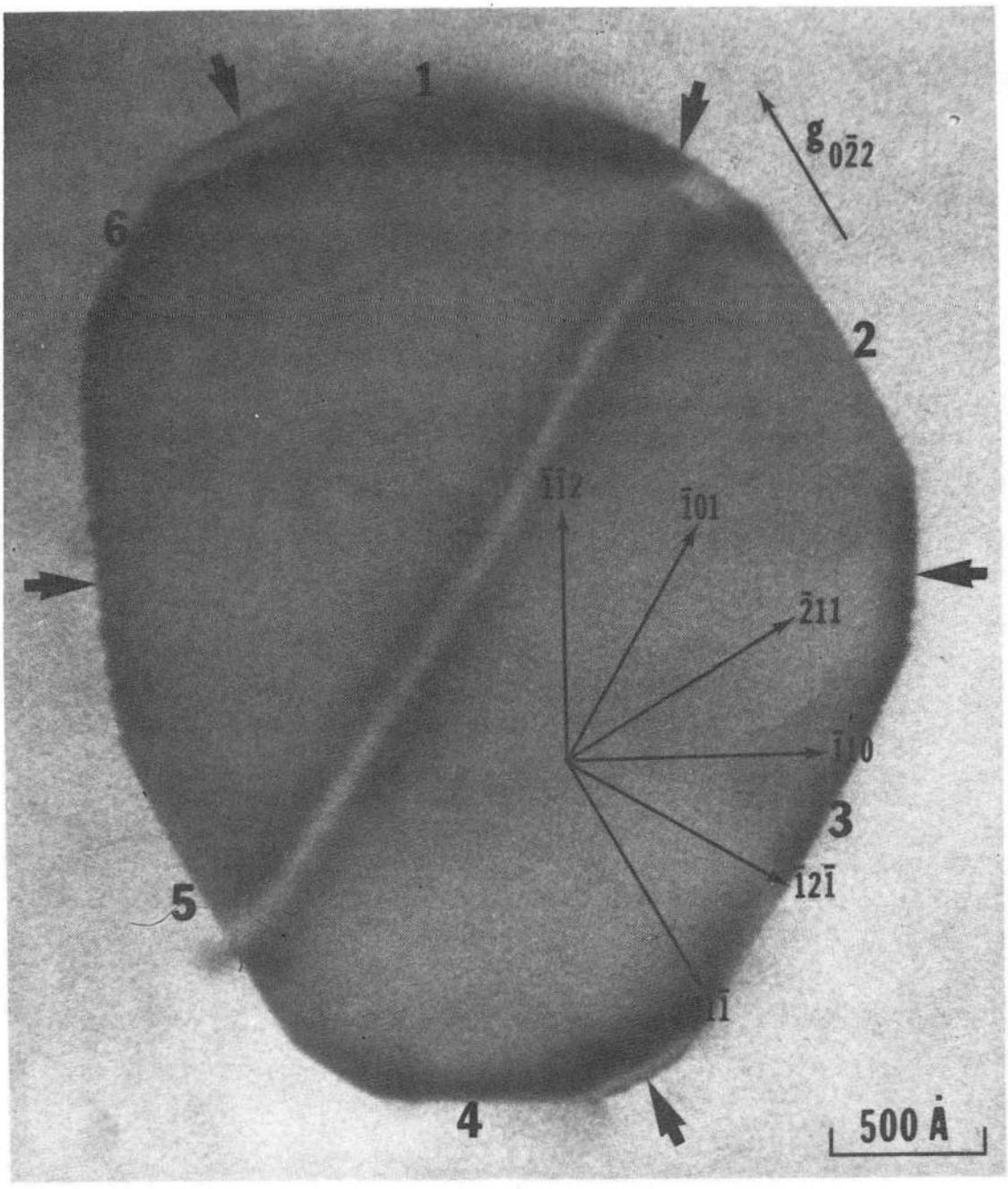

XBB 838-6704

Fig. 8

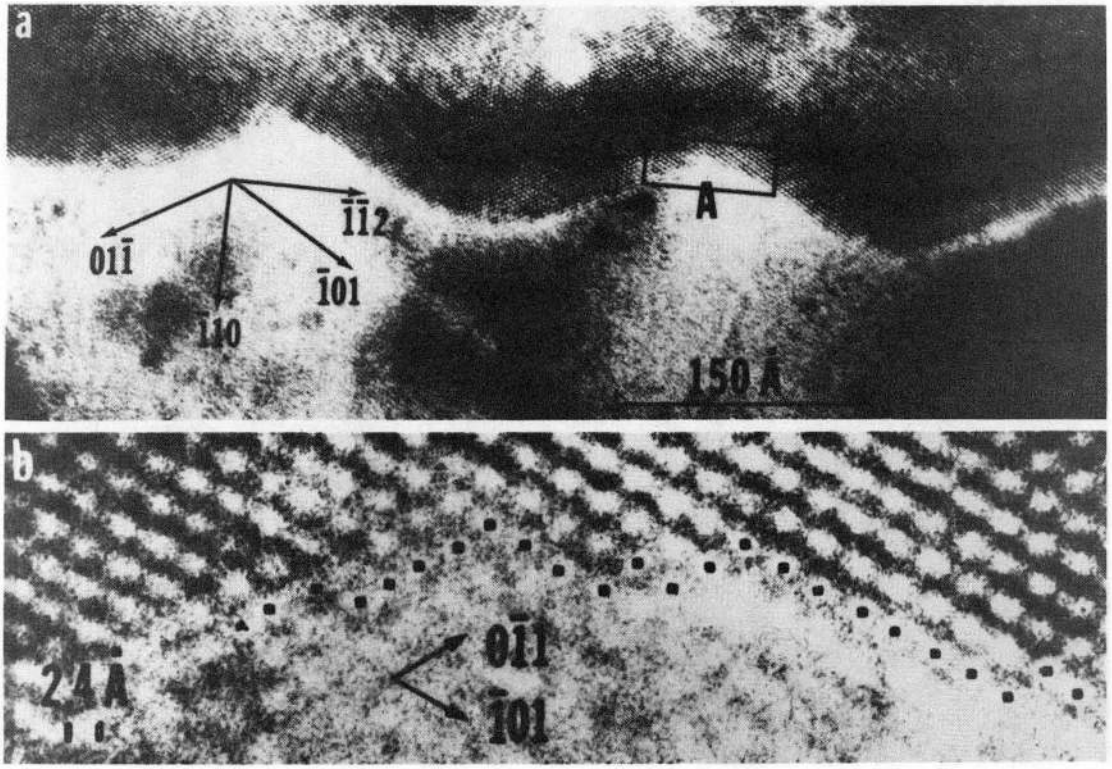

XBB 857-5317-B

Fig. 9

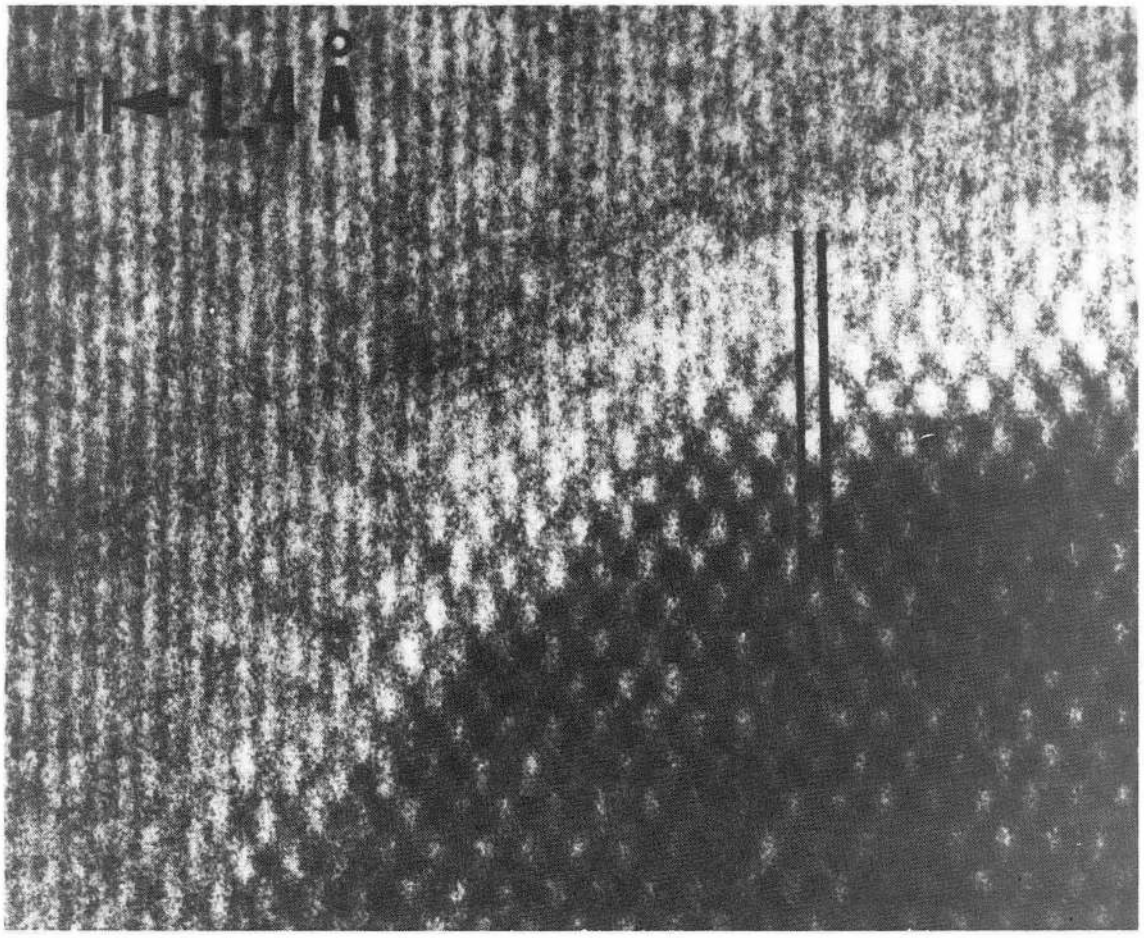

XBB 842-1204

Fig. 10

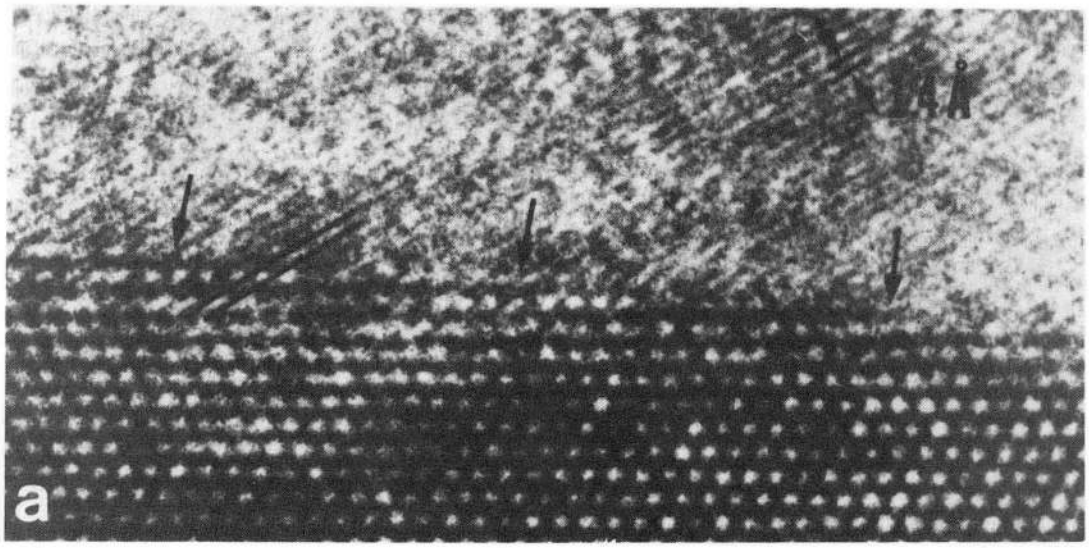

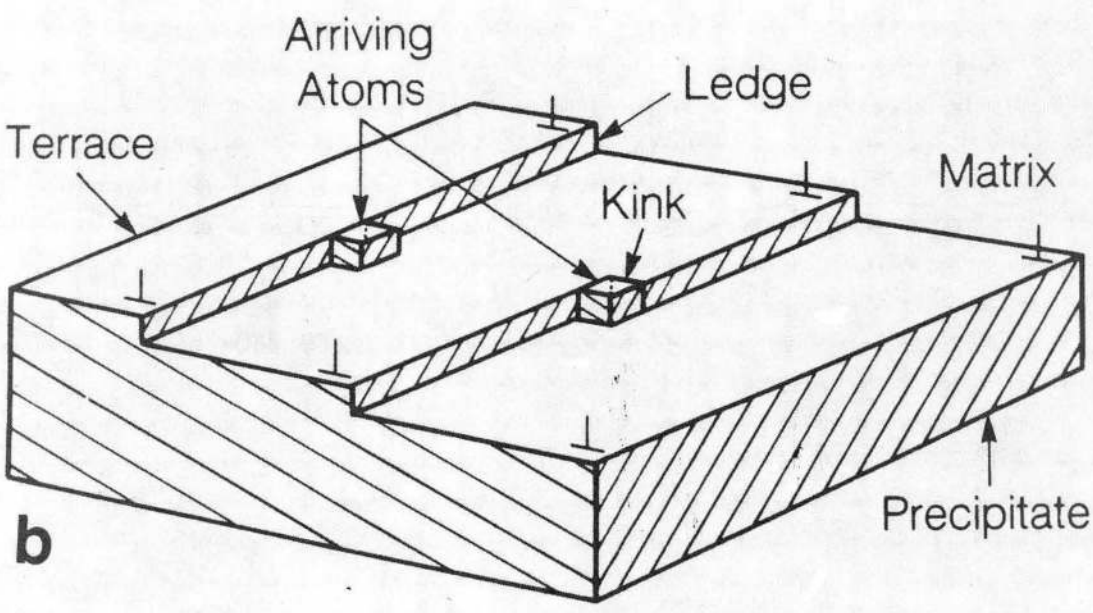

XBB 842-1205-A

Fig. 11

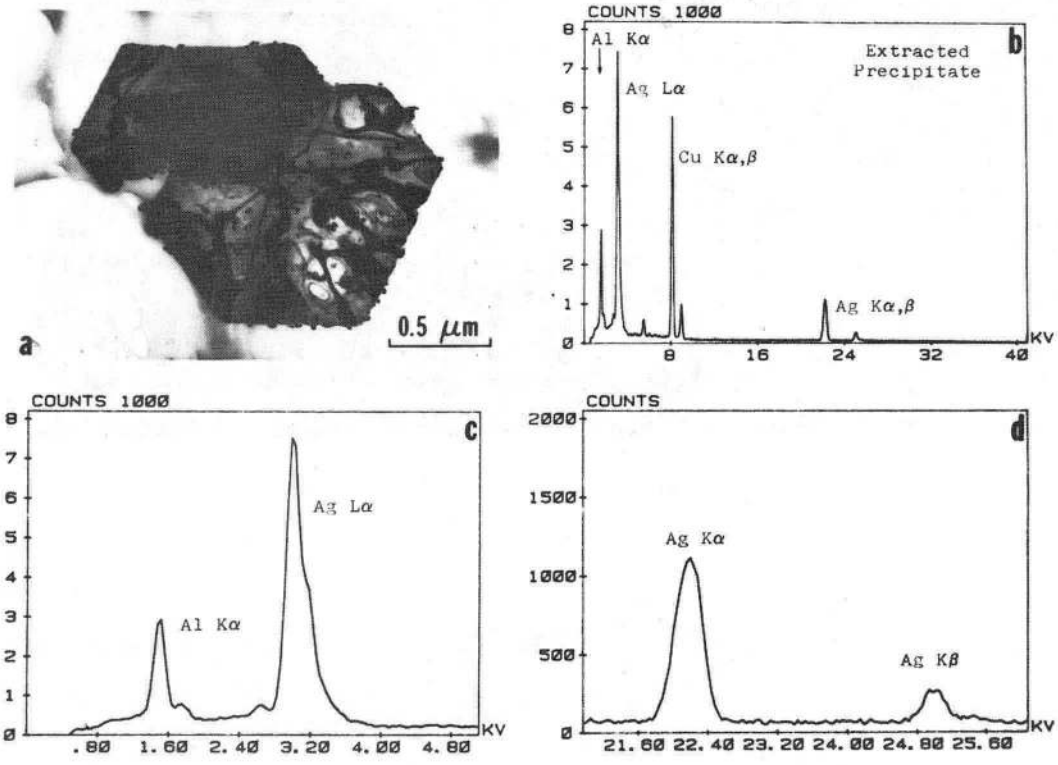

XBB 840-7663

Fig. 12

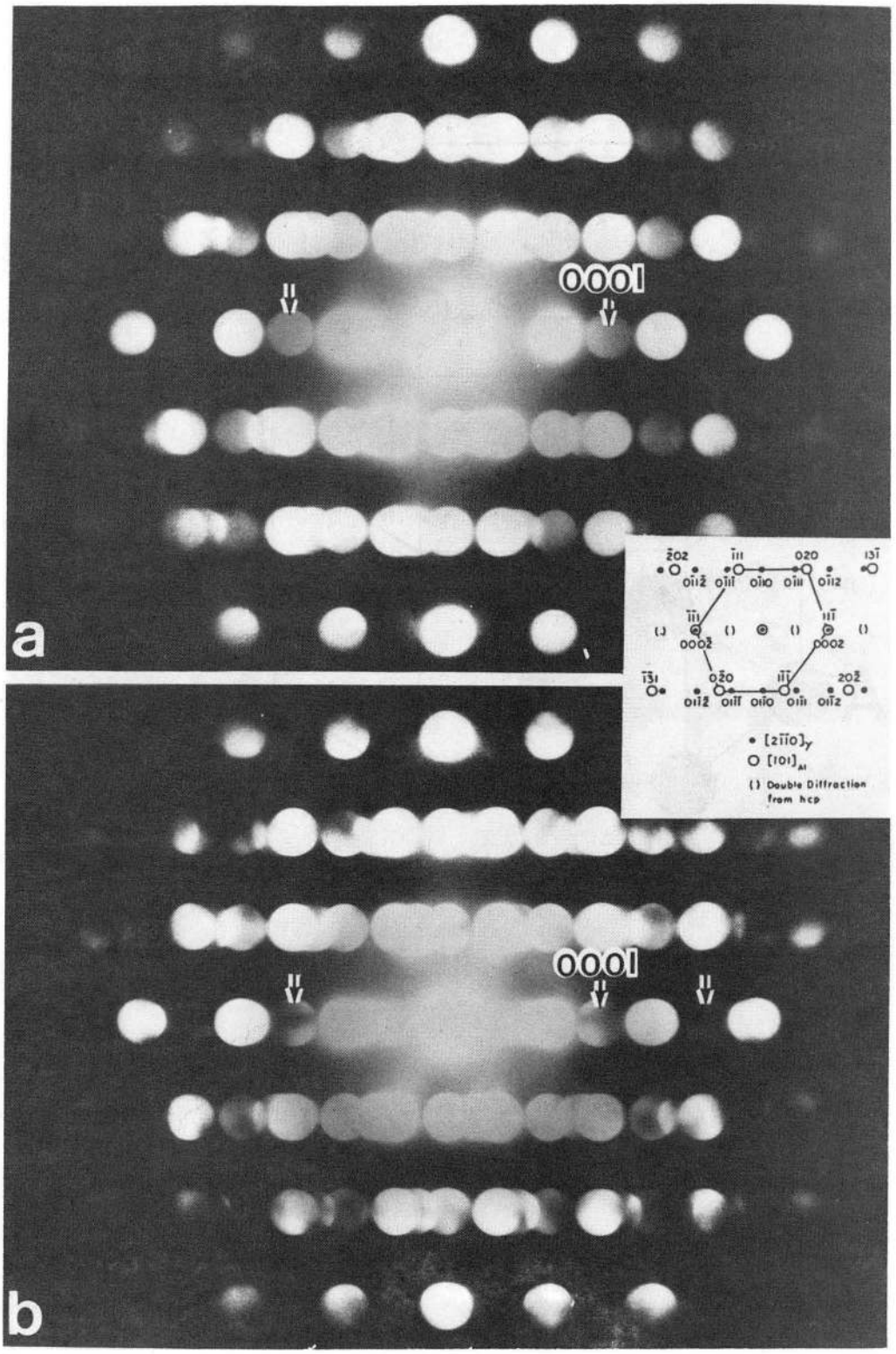

XBB 856-5646A

Fig. 13

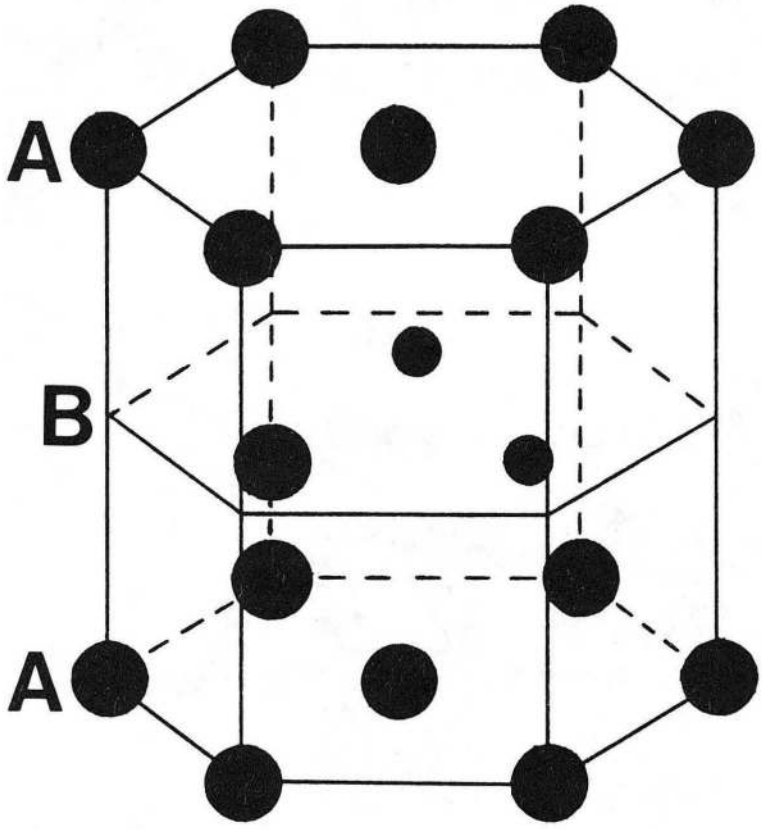

γ′

Ag

Al

XBL 865-1892

Fig. 14

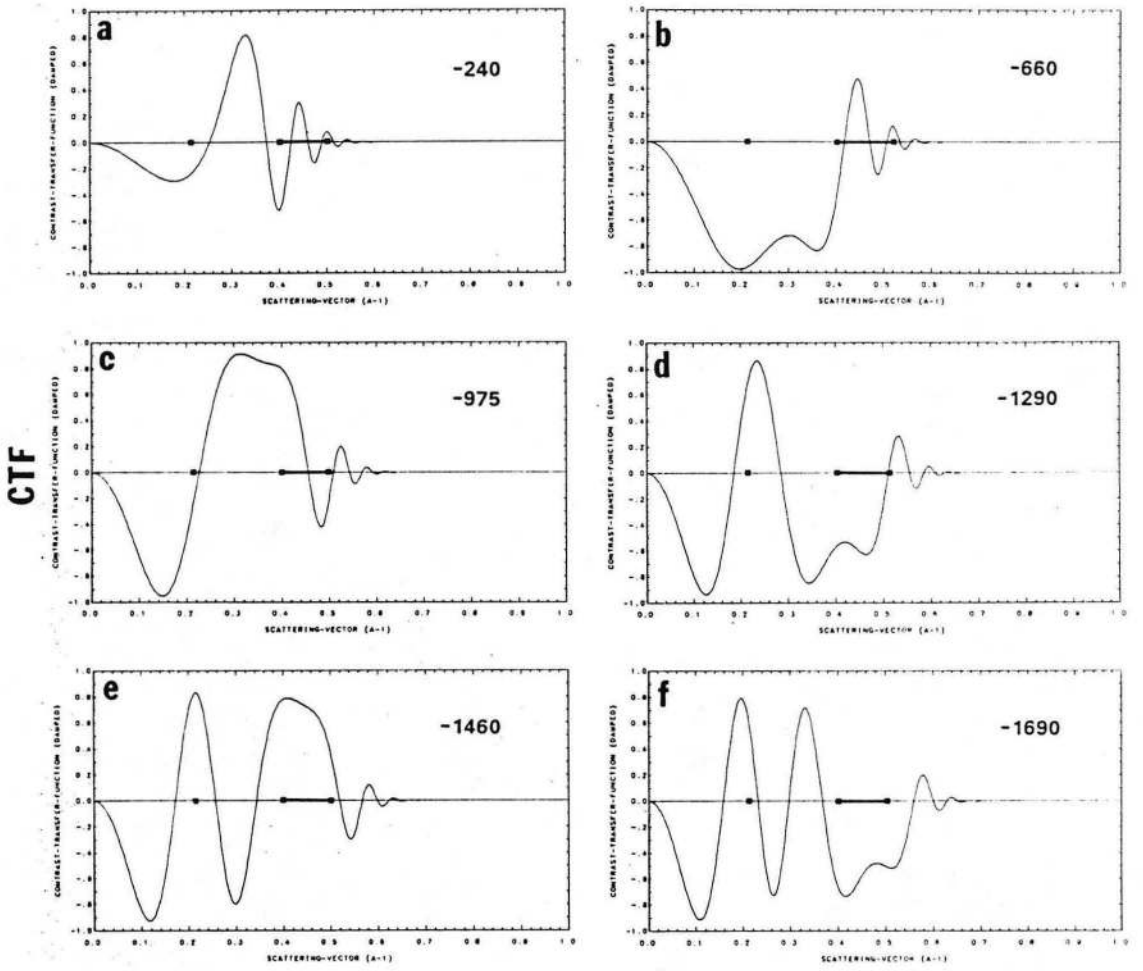

XBL 863-1061

Fig. 15

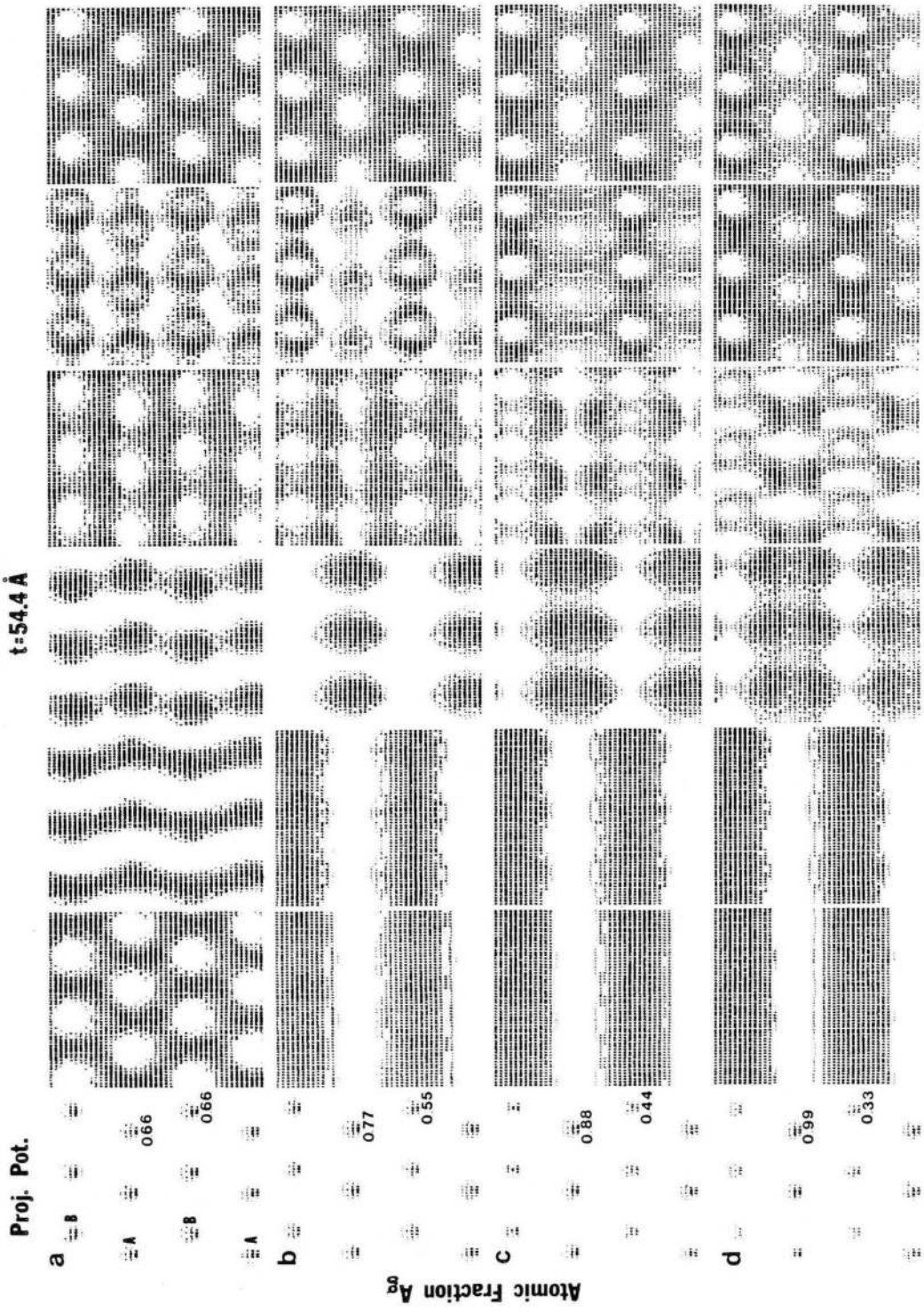

Fig. 16

XBL 852-1382

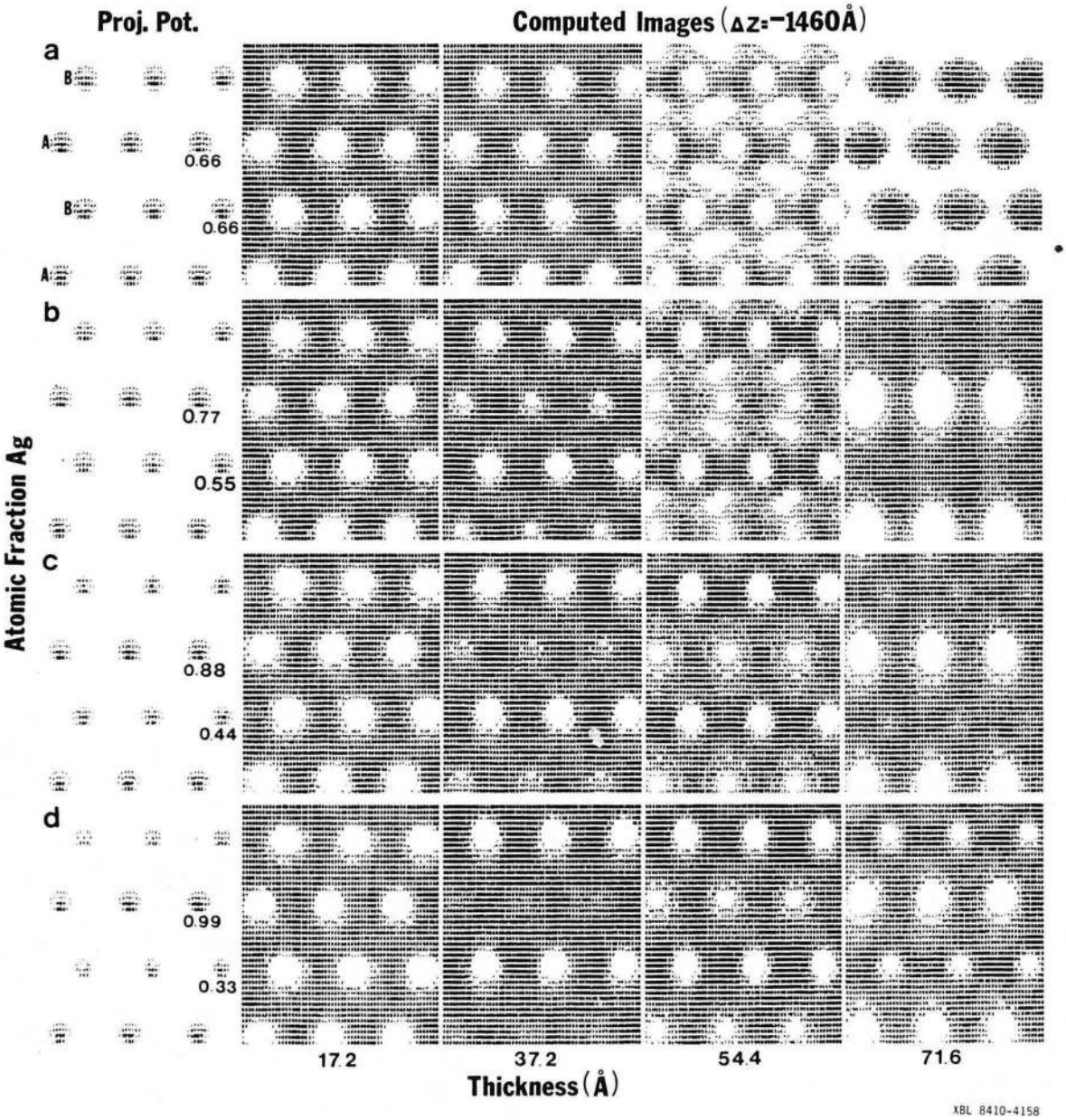
Proj. Pot.
Computed Images (Δz=-1460Å)
a
B
A
0.66
B
0.66
A
b
0.77
0.55
c
0.88
0.44
d
0.99
0.33
Atomic Fraction Ag
17.2
37.2
54.4
71.6
Thickness (Å)
XBL 8410-4158

Fig. 17

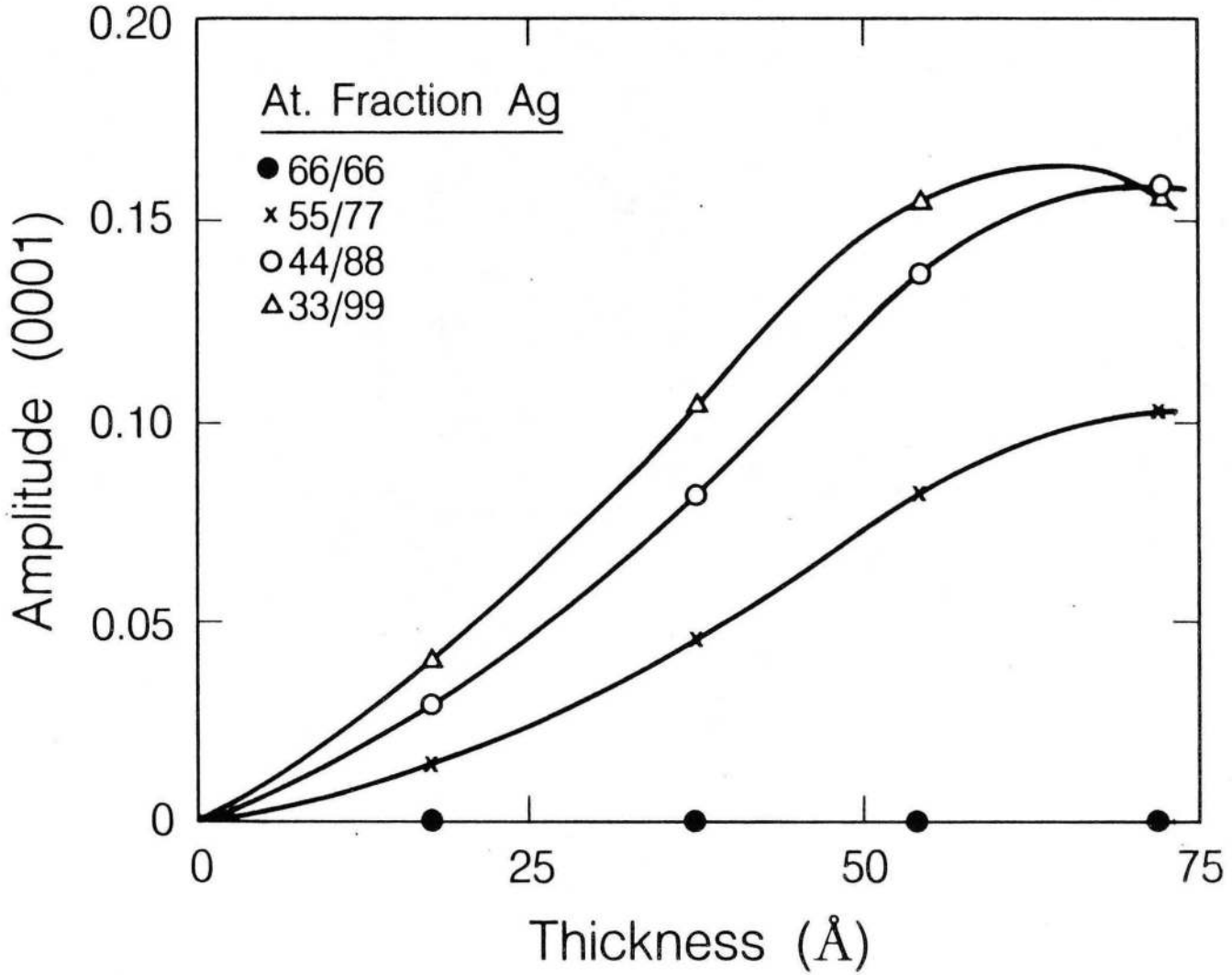

XBL 852-9754

Fig. 18

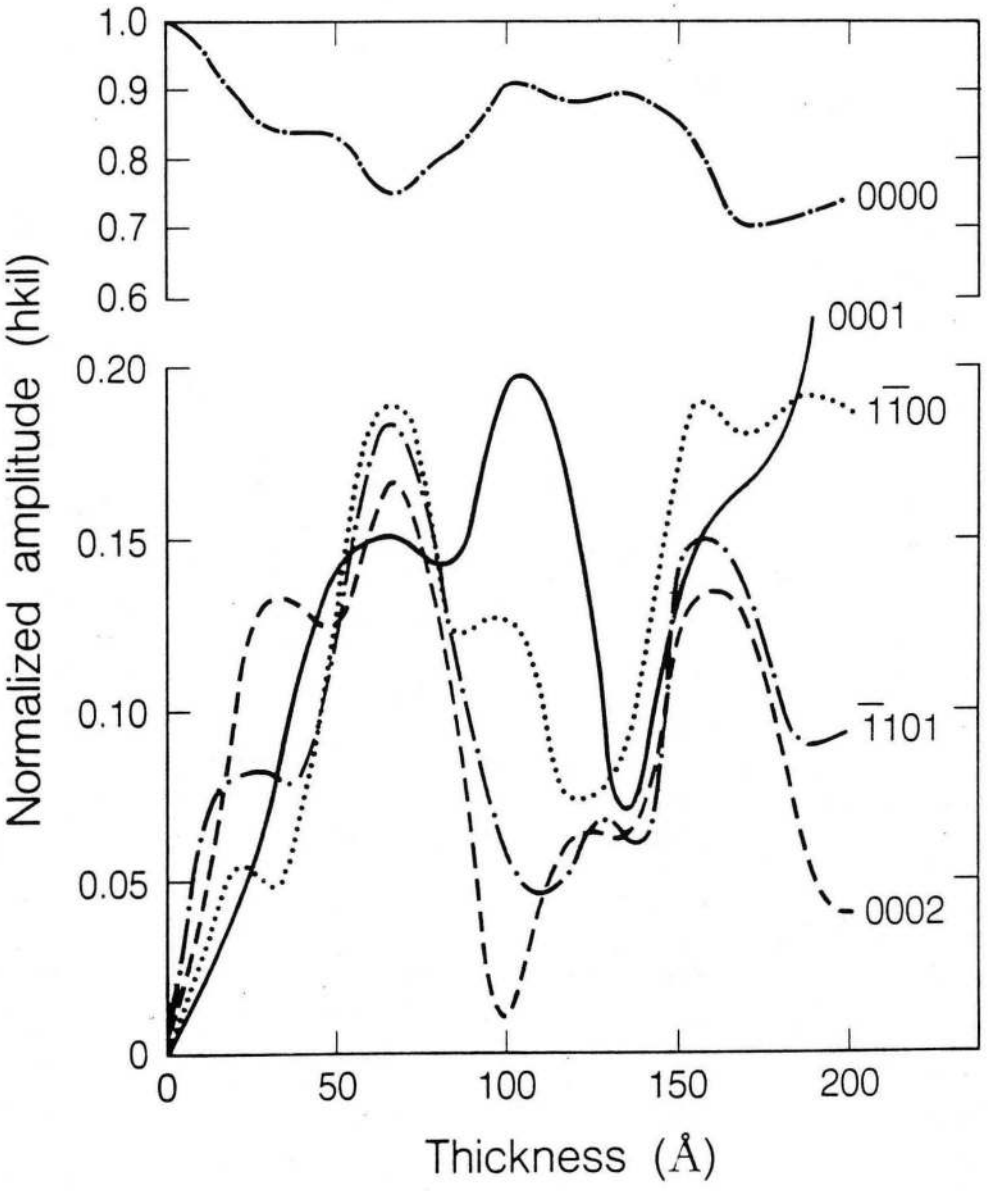

XBL 852-9755

Fig. 19

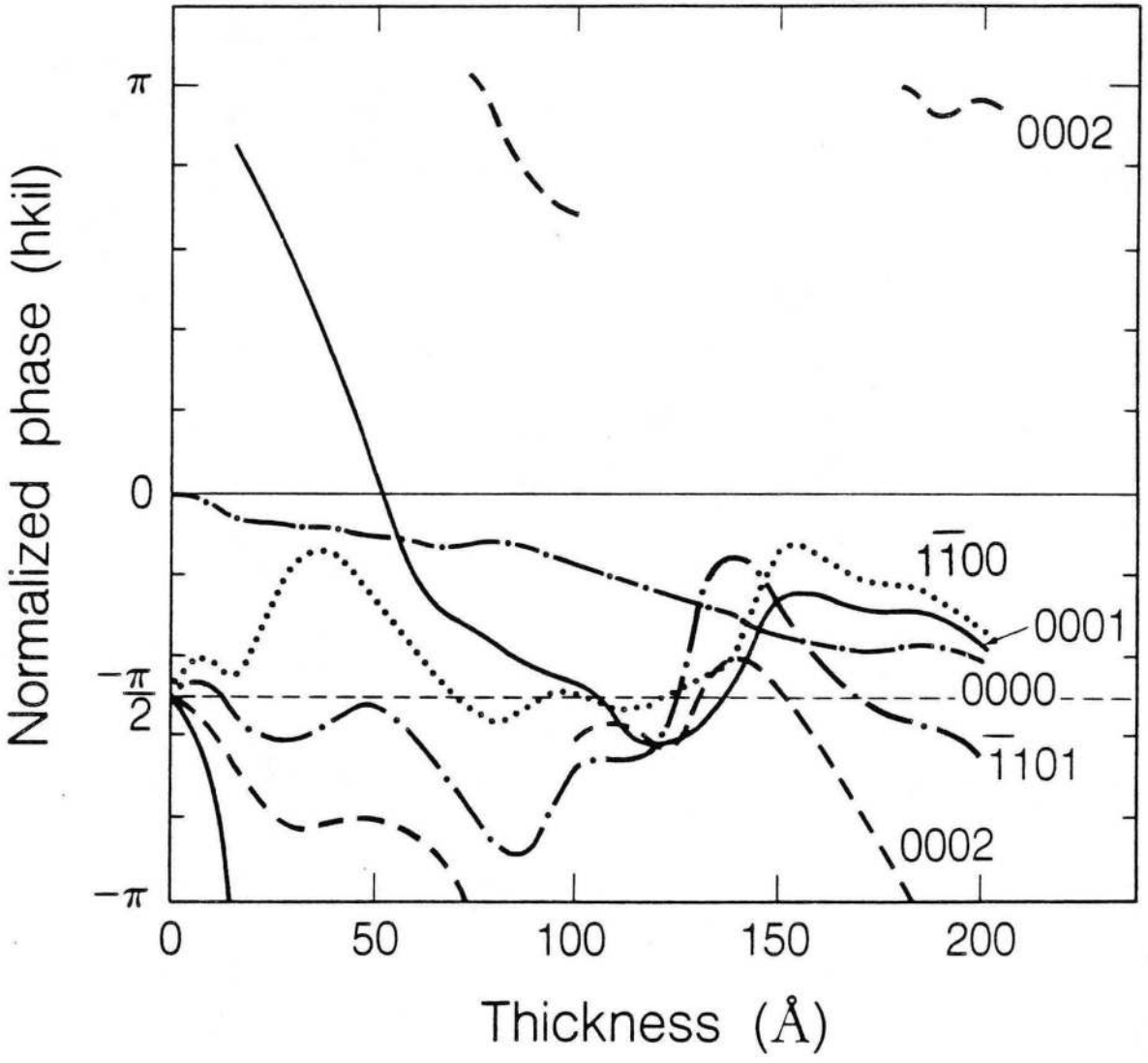

XBL 852-9756

Fig. 20

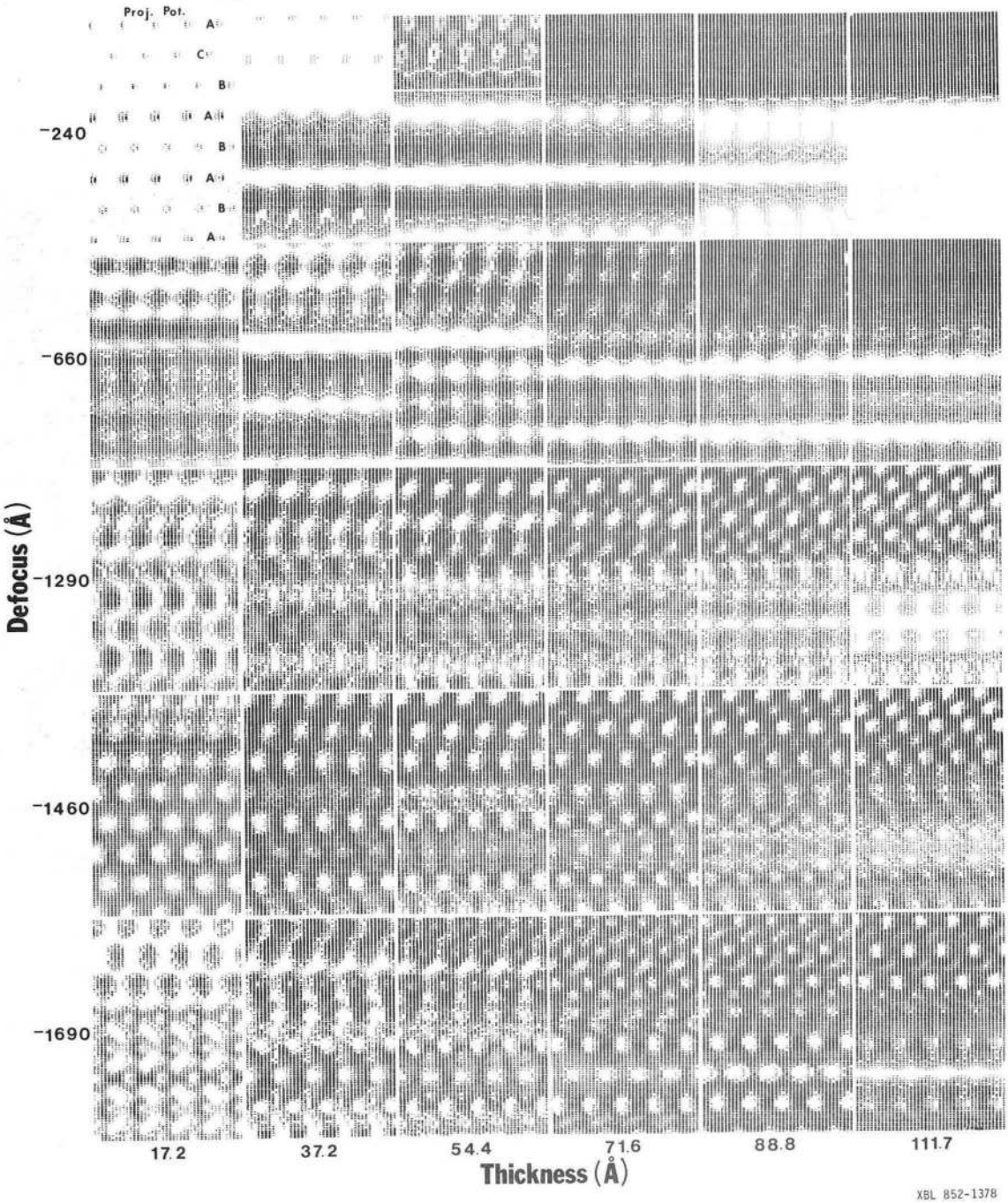
Proj. Pot.
A
C
B
A
B
A
B
A
-240
-660
-1290
-1460
-1690
Defocus (Å)
17.2
37.2
54.4
71.6
88.8
111.7
Thickness (Å)
XBL 852-1378

Fig. 21

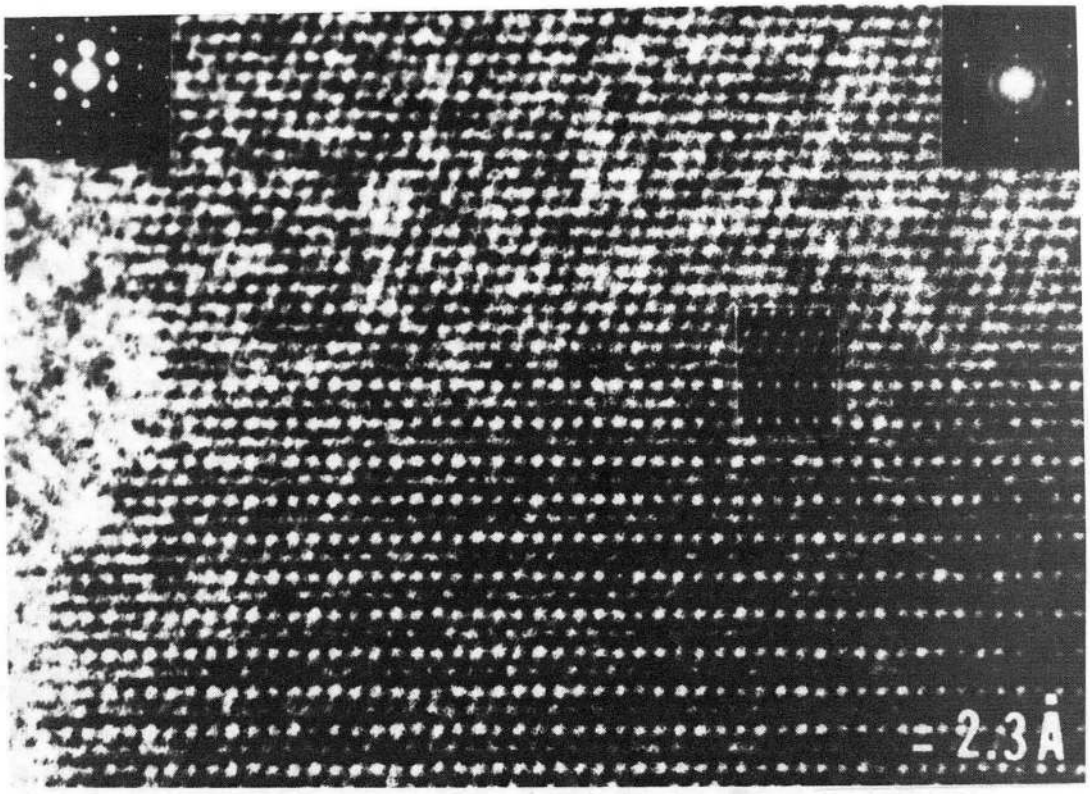

XBB 846-4293

Fig. 22

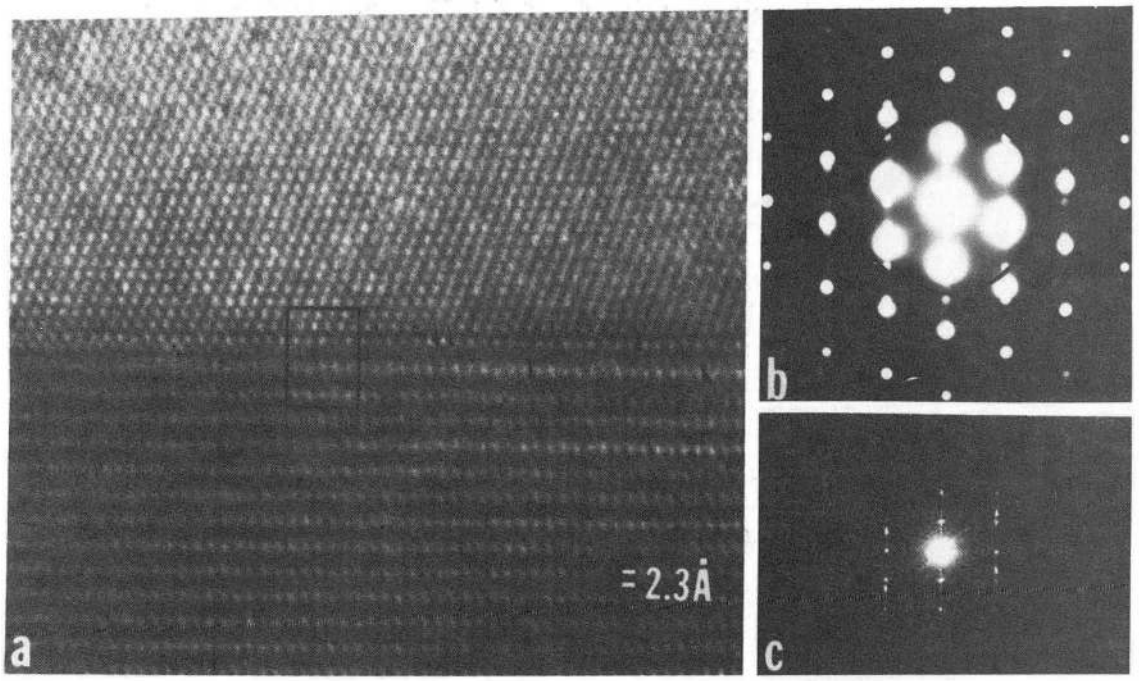

XBB 852-1545

Fig. 23

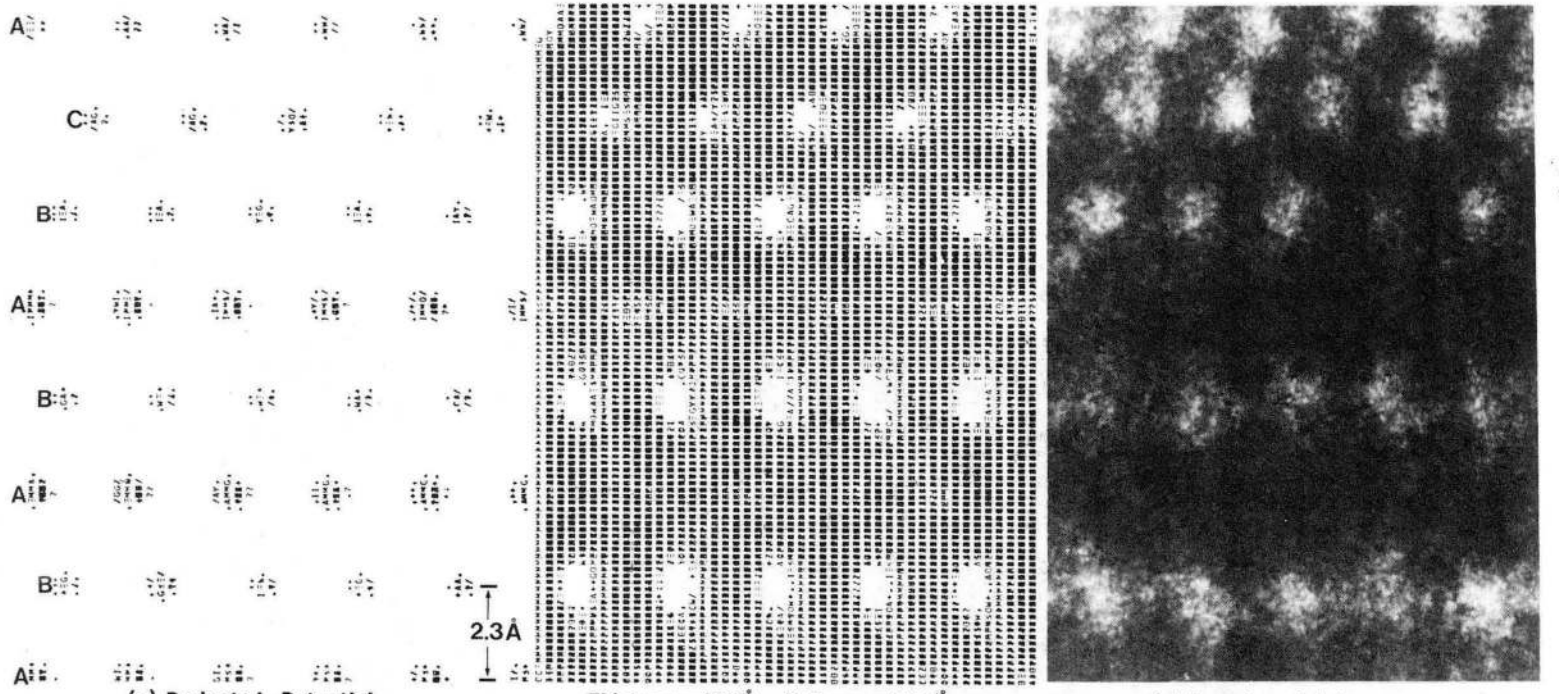

(a) Projected Potential

Thickness = 40.1Å, Defocus = -1460Å
(b) Computed Image

(c) Experimental Image

XBB 842-1226

Fig. 24

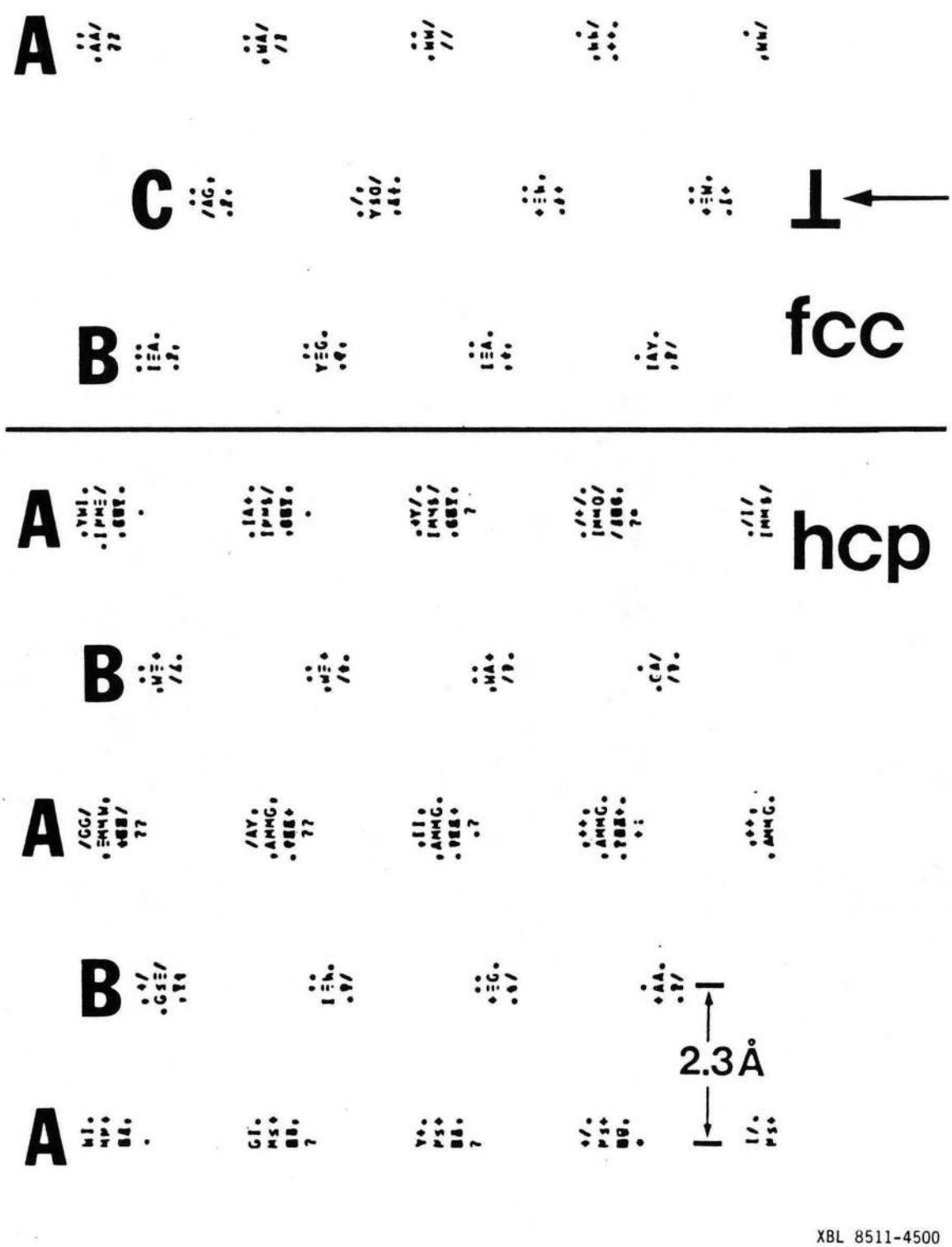

XBL 8511-4500

Fig. 25

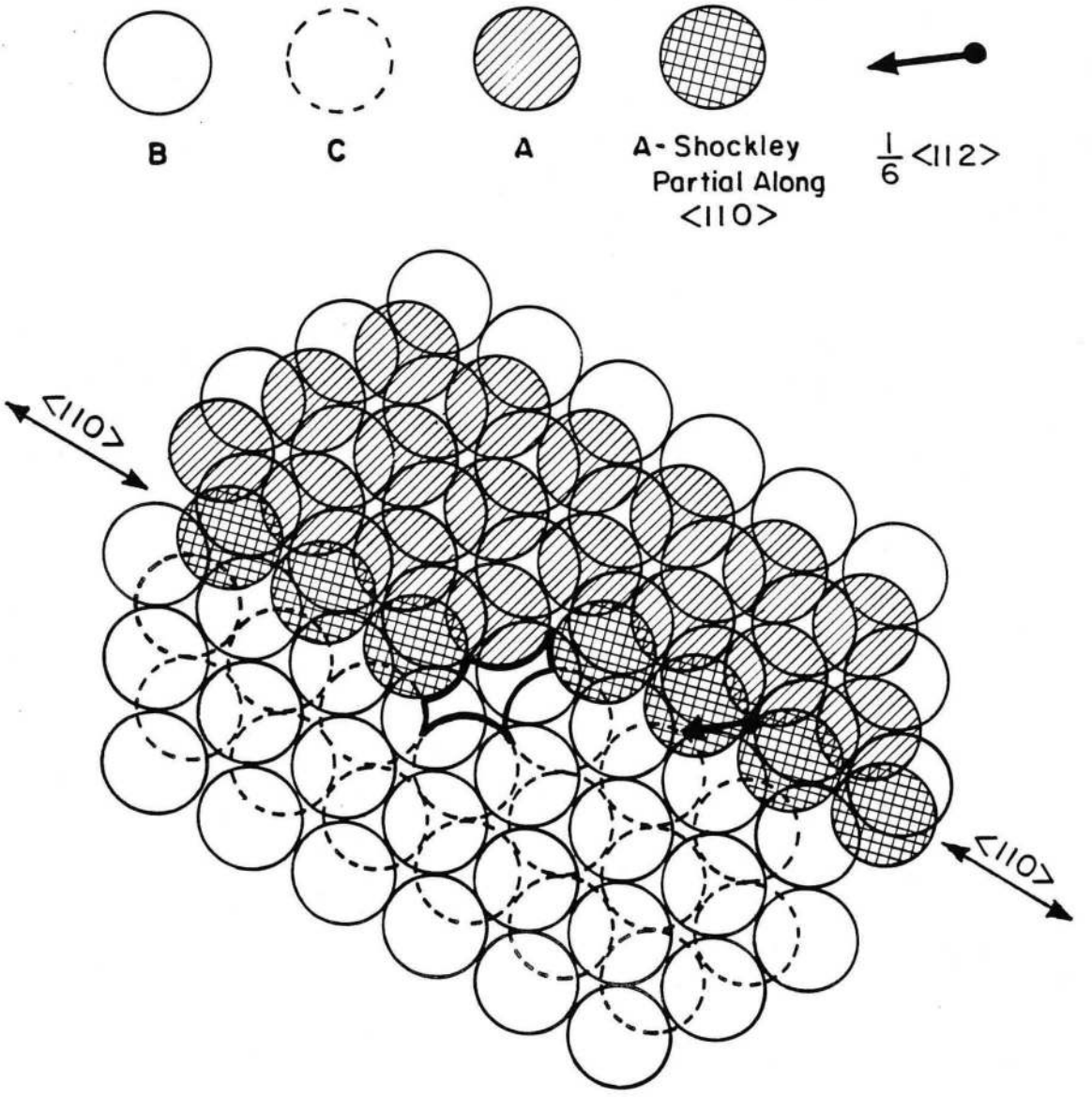

Fig. 26

LAWRENCE BERKELEY LABORATORY
TECHNICAL INFORMATION DEPARTMENT
UNIVERSITY OF CALIFORNIA
BERKELEY, CALIFORNIA 94720